# Topology optimization of modulated and oriented periodic microstructures by the homogenization method

Grégoire Allaire, Perle Geoffroy-Donders, Olivier Pantz

▶ **To cite this version:**

Grégoire Allaire, Perle Geoffroy-Donders, Olivier Pantz. Topology optimization of modulated and oriented periodic microstructures by the homogenization method. Computers & Mathematics with Applications, 2019, 78, pp.2197-2229. hal-01734709v2

**HAL Id: hal-01734709**
**https://hal.science/hal-01734709v2**

Submitted on 22 Aug 2018

**HAL** is a multi-disciplinary open access archive for the deposit and dissemination of scientific research documents, whether they are published or not. The documents may come from teaching and research institutions in France or abroad, or from public or private research centers.

L'archive ouverte pluridisciplinaire **HAL**, est destinée au dépôt et à la diffusion de documents scientifiques de niveau recherche, publiés ou non, émanant des établissements d'enseignement et de recherche français ou étrangers, des laboratoires publics ou privés.

# Topology optimization of modulated and oriented periodic microstructures by the homogenization method

Grégoire Allaire* Perle Geoffroy-Donders† Olivier Pantz‡

August 10, 2018

**Abstract**

This paper is concerned with the topology optimization of structures made of periodically perforated material, where the microscopic periodic cell can be macroscopically modulated and oriented. The main idea is to optimize the homogenized formulation of this problem, which is an easy task of parametric optimization, then to project the optimal microstructure at a desired lengthscale, which is a delicate issue, albeit computationally cheap. The main novelty of our work is, in a plane setting, the conformal treatment of the optimal orientation of the microstructure. In other words, although the periodicity cell has varying parameters and orientation throughout the computational domain, the angles between its members or bars are conserved. The main application of our work is the optimization of so-called lattice materials which are becoming increasingly popular in the context of additive manufacturing. Several numerical examples are presented for compliance minimization in 2-d.

## 1 Introduction

Topology optimization of structures is nowadays a well developed field with many different approaches and a wealth of applications. One of the earliest method of topology optimization was the so-called homogenization method, introduced in the early eighties by mathematicians [14], [15], [17] (see the textbook [1] for more references), and popularized by the seminal paper [7] which was the first one to numerically treat a realistic problem in the elasticity setting (the previous numerical works were restricted to an anti-plane elasticity setting, namely a scalar equation). Despite its great success, the homogenization method progressively faded away because it was surpassed by a less rigorous method, but much simpler and as efficient in most cases, the so-called SIMP

*CMAP, École Polytechnique, Palaiseau, FRANCE – gregoire.allaire@polytechnique.fr
†Safran Tech, Magny-les-Hameaux, France – perle.geoffroy@polytechnique.edu
‡Université Côte d'Azur, LJAD, FRANCE – pantz@unice.fr

method introduced in [6], [23] (see the textbook [8] for a more complete account). The SIMP method is said to be less rigorous because it uses fictitious isotropic materials while the homogenization relies on true composite materials, possibly anisotropic. However, as soon as penalization of intermediate densities is put in action, there is no need of using true composite materials, which have complicated effective properties and require much more modeling and computational efforts than the simple material interpolation involved in SIMP. This is the key for the immense popularity of SIMP which is the most commonly used method in commercial topology optimization softwares.

However, the appearance of mature additive manufacturing technologies which are able to build finely graded microstructures (sometime called lattice materials) may drastically change the picture and we could well see a resurrection of the homogenization method for such applications. Indeed, homogenization is the right technique to deal with microstructured materials where anisotropy plays a key role, a feature which is absent from SIMP. Homogenization theory allows to replace the microscopic details of the structure (typically a complex networks of bars, trusses and plates) by a simpler effective elasticity tensor describing the mesoscopic properties of the structure. Therefore, the analysis of the structure is greatly accelerated since there is no need to mesh or represent on a fixed mesh all the microscopic details of its shape. There is however one final hurdle, once an optimal composite structure has been obtained, which is the projection of the optimal microstructure at a chosen finite lengthscale to get a global and detailed picture of the optimal microstructure. This is the most delicate part of this homogenization approach and the one where the present paper is most contributing.

We follow the lead of the pioneering paper [18] which was the first to propose such a post-treatment of the homogenization method in topology optimization. The main idea is to project the optimal microstructure on a fine mesh of the overall structure in a smoothly varying way. This implies that locally the microstructure is deformed and oriented to adapt to its macroscopic variations. We depart from the work [18] and improve it in several aspects.

First, in [18], rank-two laminates were used during the optimization process. The advantage is that such rank-two laminates have explicit effective properties and are known to be optimal for 2-d compliance minimization. The drawback is that they are difficult to manufacture since they are featuring two well separated lengthscales. To circumvent this problem, during the post-processing or projection step, those rank-two laminates were arbitrary replaced by periodic composites, whose behavior are close – but still different – from the rank-2 laminates used during the optimization stage. As a consequence, the sequence of projected shapes were not exactly converging toward the computed optimal composite shape. In the present article, we lift this inconsistency. At all stages of our method, we use the same microstructure, namely periodic square cells with rectangular holes like in [7]. Other parametrized periodicity cell would be acceptable in our approach (see [10] for other examples, including triangular or hexagonal cells).

Second, in [18], rectangular and squared cells were assumed to behave simi-

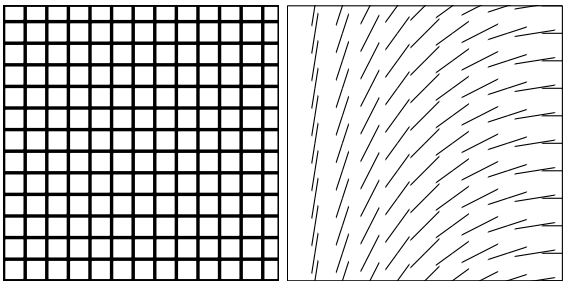

(a) Regular grid (b) Direction field

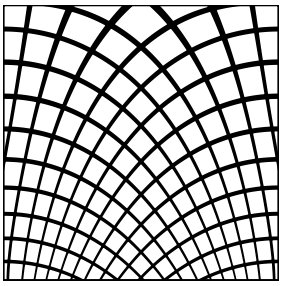

(c) Distorted grid

Figure 1: A regular grid (a) is associated to a direction field (b), giving the local orientation of each cell: it yields a distorted grid (c)

larly. This simplified greatly the projection step. Here, we do not make such an approximation. We construct a sequence of genuine shapes based on a square lattice. As a consequence, we have to enforce a conformality property to the underlying lattice of the periodic composite, namely that, after deformation and orientation, right angles in the microstructures should stay right angles (see Figure 1). Note that a side effect of the conformality condition is that it imposes to the rotation field of the cells to be harmonic and thus regular. In [18], a different regularization was applied.

Third, we have greatly simplified the projection step. A major obstacle is related to the fact that the orientation of the cells are only defined up to a rotation of angle $\pi$. In [18], a quite unnatural trick was used to get over this problem. It led to a verbose formulation during the regularization step of the orientation of the cells. We propose here a different solution that consists in replacing the computational domain by an abstract manifold. It is worthy to note that our method is ready to use in the presence of singularities of the lattice, that is when no coherent orientation of the cells does exist (see [19]). Eventually, in a last post-processing operation, we clean the projected structure by removing disconnected bars or bars that have a free hanging end point.

At this point, let us mention the recent work [11] which is proposing yet another homogenization method in the spirit of [18].

The content of this paper is the following. Section 2 is devoted to a presentation of our setting. We focus on 2-d compliance minimization for a single load state equation (the generalization to other objective functions, multiple load problems, or 3-d requires additional ideas, see [10]). We briefly recall the necessary ingredients of the homogenization approach and we explain our three-steps strategy. First, choose a parametrized periodicity cell and pre-compute its effective properties for the entire range of its parameters. Second, perform a topology optimization of the composite structure, which turns out to be a simple parametric optimization problem since our periodicity cell is parametrized. Third, apply a post-processing step which amounts to project, at a specified lengthscale, a modulated and oriented periodicity cell.

Section 3 deals with the pre-processing step of computing the effective properties of our parametrized periodicity cell which, here, is a square cell with a rectangular holes (thus having two parameters for the hole, on top of the orientation angle). We recall the homogenization formulas, based on the notion of cell problems [1] and we compute the derivatives, with respect to the parameters, of the effective or homogenized tensor.

Section 4 deals with topology optimization for a 2-d compliance problem with a set of admissible designs which are the homogenized tensors of Section 3. Therefore, it is a parametric optimization problem and solving it is quite standard. Here we rely on a projected gradient algorithm for the hole parameters and optimality criteria for its orientation.

Section 5 is the main novelty of the present work, devoted to the post-processing of the homogenized result of Section 4, namely the projection of the optimal microstructure. Section 5.1 defines the way the microscopic cell is macroscopically modulated. First, the cell parameters (more precisely the width and height of the rectangular hole, see Figure 2) vary from point to point in the computational domain. Second, the orientation of the periodicity cell varies too. More precisely, we introduce a vector field $\varphi(x)$, the inverse of which maps the periodic square grid on a distorted grid where each cell is optimally oriented (see Figure 1). Section 5.2 introduces a conformality condition to be satisfied by the grid map $\varphi$ so that right angles in the original square grid remain right angles in the deformed configuration. As proved in Lemma 5.1 this is equivalent for the orientation angle $\alpha$ to be harmonic (in two space dimensions). Section 5.3 explains how the orientation angle $\alpha$ is optimized for mechanical performance and slightly regularized. Section 5.4 is the heart of our approach: there, the grid map $\varphi(x)$ is deduced from the optimal angle $\alpha(x)$. Section 5.5 gives all the necessary computational details on how to find the grid map $\varphi$ in practice. Section 5.6 gives the numerical results obtained with our approach. Eventually, Section 5.7 is devoted to a last "cleaning" step of the projected structure where disconnected bars or bars that have a free hanging end point are automatically removed.

Section 6 gives numerical examples of the whole process applied to other test cases including an arch, a cantilever, a MBB beam and a L-beam. We also present an example featuring singularities in the orientation field which can not be treated by our current implementation of the proposed algorithm. Never-

theless, a more careful regularization of the orientation allows us to remove the singularities and give a satisfactory optimal design. The complete description of how to remove the singularities will be the topic of a future work [10].

# 2 Setting of the problem

## 2.1 Topology Optimization

Let $D \subset \mathbb{R}^N$ be a fixed smooth bounded open set (the working domain) and $\Omega \subset D$ the reference configuration of an isotropic elastic body. The structure $\Omega$ is clamped on $\Gamma_D \subset \partial\Omega$, and submitted to surface loads $g$ on $\Gamma_N \subset \partial\Omega$. For simplicity these parts $\Gamma_D$ and $\Gamma_N$ of the boundary are assumed to be fixed and subsets of $\partial D$. We assume that the solid is made of an homogeneous isotropic linear elastic material of Hooke's law $A$, with Lamé coefficients $\lambda$ and $\mu$. The displacement $u$ and the stress tensor $\sigma$ are then solution of the system

$$\begin{cases} \operatorname{div}(\sigma) = 0 & \text{in } \Omega, \\ \sigma = Ae(u) & \text{in } \Omega, \\ u = 0 & \text{on } \Gamma_D, \\ \sigma \cdot n = g & \text{on } \Gamma_N, \\ \sigma \cdot n = 0 & \text{on } \Gamma = \partial\Omega \setminus (\Gamma_D \cup \Gamma_N), \end{cases}$$

where $e(u) = \frac{1}{2}(\nabla u + \nabla u^T)$ is the strain tensor (the symmetrized gradient of the displacement).

Shape and topology optimization consists to determine the domain $\Omega$ that minimizes a given objective function $J$,

$$\begin{array}{c} \min \quad J(\Omega) \\ |\Omega| \leq V, \\ \Gamma_D \cup \Gamma_N \subset \partial\Omega \end{array} \tag{1}$$

where $V \in \mathbb{R}^+$ is the maximum admissible volume. A typical objective function is the compliance

$$J(\Omega) = \int_{\Gamma_N} g \cdot u \, ds \, .$$

For most cost functions $J$, problem (1) does not admit a solution [1]. This is due to the fact that composite shapes, made of very small microstructures, can always outperform genuine shapes made of plain material. A composite shape is described by the local density $\theta(x)$ of material and a homogenized elasticity tensor $A^*(x)$ that depends on the microstructure at the point $x \in D$. The homogenized or macroscopic displacement $u^*$ of the structure is then solution of the system

$$\begin{cases} \operatorname{div}(\sigma) = 0 & \text{in } D, \\ \sigma = A^* e(u^*) & \text{in } D, \\ u^* = 0 & \text{on } \Gamma_D, \\ \sigma \cdot n = g & \text{on } \Gamma_N, \\ \sigma \cdot n = 0 & \text{on } \Gamma = \partial D \setminus (\Gamma_D \cup \Gamma_N). \end{cases}$$

We emphasize that the problem is now defined on the whole working domain $D$ and no longer on a shape $\Omega$. Then, the minimization problem should be rewritten as a minimization problem of a relaxed cost function $J^*$ with respect to the homogenized elasticity tensor $A^*$ and the density $\theta$

$$\min_{\substack{\int_D \theta \leq V, \\ A^*(x) \in G_\theta(x)}} J^*(\theta, A^*)\,. \tag{2}$$

where $G_\theta(x)$ is the set of effective or homogenized Hooke's laws for microstructures of density $\theta(x)$. The main difficulties in the homogenized formulation (2) are, first, to compute the relaxed cost function $J^*$ (which may be different from the original cost function $J$), second and most importantly, to give a complete and explicit description of the set of admissible Hooke's laws $G_\theta$. It is only for special cases (like compliance minimization) that (2) can be made fully explicit [1]. Furthermore, composite shapes are only mathematical ideal objects. They can not be actually build as they are made of infinitely small details. To circumvent these obstacles, following the lead of [18], we propose to limit the set of admissible composites to microstructures for which the Hooke's law can be numerically computed (typically, periodic composites with a square cell). Finally, we do not seek for the optimal homogenized or composite solution but for a sequence of genuine non composite shapes containing more and more details that does converge toward the optimal composite solution.

## 2.2 A three steps approach

Our goal is to construct a minimizing sequence for (2), where the homogenized tensors $A^*$ are restricted to a specific class of composite materials. By minimizing sequence, we mean a sequence of classical or genuine shapes which converges to the infimum value of (2), and which is indexed by its lengthscale (or periodicity) $\varepsilon > 0$, a small parameter going to zero. To achieve this goal, our main strategy is to follow a three step approach. First, choosing a parametrized class of composite materials, we determine the subset of homogenized Hooke's laws for these allowed composite shapes, when their parameters vary. Second, we solve the relaxed or homogenized formulation (2) when the full set $G_\theta$ is replaced by its subset numerically found during the first step. This is typically a rather easy parametric optimization problem. Third, and most importantly, we construct a sequence of genuine shapes that does converge toward the optimal composite found during the second step. This last step is a rather computationally cheap post-processing of the previous step but it is where we put our main modeling and algorithmic efforts.

We restrict our analysis to the two dimensional case ($N = 2$) and to locally square-periodic composites. Note that it should be possible to adapt the whole method (or at least part of it) to hexagonal cells or to the three dimensional case. The first step consists in determining the properties of such materials when varying their parameters (see Section 3). It is a preprocessing stage which can be performed off-line and is the same, whatever the choice of objective functions,

computational domain, applied loads and boundary conditions. Hooke's laws are computed by solving cells problems that describe the deformation at the scale of the microstructure. This is a very classical task in homogenization theory. Adding a rotation is obvious and does not require additional computations.

In a second step, we compute the optimal solution of the shape optimization problem (2) over the previously found set of locally square-periodic composites (see Section 4). This is a parametric problem where the design variables are, at every point of the computational domain, the periodicity cell parameters and its orientation or angle.

Finally, the third step yields a minimizing sequence of genuine shapes, converging toward the optimal solution, and indexed by the period $\varepsilon$ (see Section 5). For each given value of $\varepsilon$, a genuine or classical shape is obtained by projecting on a mesoscopic (or even macroscopic) scale the distorted grid of the periodicity cells. To achieve this, we deduce from the optimal orientation angle, satisfying a conformality condition, a vector field or grid map. The optimal microstructure is then projected along this grid map. A final post-processing cleaning process is also applied to remove disconnected or hanging bars.

# 3 Preprocessing : homogenized Hooke's laws of the microstructures

## 3.1 Set of admissible microstructures

From now on, we restrict ourselves to the two dimensional case (see [10] for some 3-d examples) and restrain our analysis to a simple class of composites already used in the seminal paper [7] : square cells with a rectangular central hole (see Fig.1) repeated periodically on the whole space. This class of composites is parametrized by the relative linear dimensions of the hole $m = (m_1, m_2) \in [0,1]^2$, together with the orientation $\alpha$ of the cell, which is the angle made by the $y_1$-axis of the cell with the $x_1$-axis of the domain $D$. We denote the periodic cells $Y_\alpha(m)$.

The structure of those cells as well as their Hooke's laws are not very far from those of rank-2 laminates with orthogonal lamination directions, which are optimal for single-load compliance minimization problems [1]. Rank-2 laminates were used in the inspiring work [18]: however they are intrinsically multiscale (more precisely, they feature two well separated microscopic scales) and thus hard to manufacture. On the contrary, perforated square cells feature a single scale and are more likely to be additive manufacturable. We emphasize that the following method is not restricted to our choice of cells, and it can easily be extended to any other parameterizable cells. Particularly, some authors have optimized periodic cells for given objective function [12, 5] that could be good candidates.

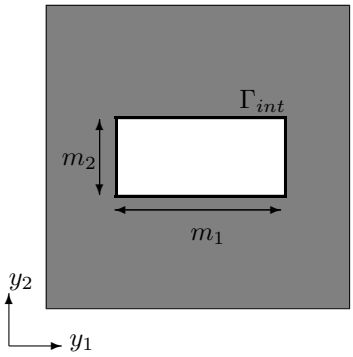


Figure 2: Periodicity cell $Y_0(m)$.

### 3.2 Cell problem and homogenized elasticity tensor

For the sake of brevity, only a few important results on the theory of homogenization are recalled here: the interested reader will find more details in [1]. Assume that, in a given macroscopic domain, there is a periodic distribution of holes inside an isotropic elastic solid phase, with constant elasticity tensor $A$. The periodicity size is denoted by $\varepsilon > 0$. The rescaled periodicity cell is the unit cube $(0,1)^2$. Inside this unit periodicity cell, the solid domain is the subset $Y_0 \subset (0,1)^2$, its complement being holes with boundaries $\Gamma_{int}$. When $\varepsilon \to 0$, the medium can be considered homogeneous, with an effective constant elasticity tensor $A^*$. To compute this homogenized tensor $A^*$, one needs so-called correctors $w_{ij}$, corresponding to the local displacements in the cell $Y_0$, defined for each pair $(i,j) \in \{1,2\}^2$ as the solutions of the following *cell problems*

$$\left\{ \begin{array}{cc} \mathrm{div}(A(e_{ij} + e(w_{ij}))) = 0 & \text{in } Y_0 \\ A(e_{ij} + e(w_{ij}))n = 0 & \text{on } \Gamma_{int} \\ y \mapsto w_{ij}(y) & (0,1)^2\text{-periodic} \end{array} \right. \tag{3}$$

where $e_{ij} = \frac{1}{2}(e_i \otimes e_j + e_j \otimes e_i)$ is a basis of the symmetric tensors of order 2, and $n$ is the normal to the hole's boundary $\Gamma_{int}$ in $Y_0$. The variational formulation of the cell problem (3) is: find $w_{ij} \in H^1_{\#}(Y_0, \mathbb{R}^2)$ such that

$$\forall \phi \in H^1_{\#}(Y_0, \mathbb{R}^2) \quad \int_{Y_0} Ae(w_{ij}) : e(\phi) + \int_{Y_0} Ae_{ij} : e(\phi) = 0\,, \tag{4}$$

which admits a unique solution (up to an additive translation). The tensor $A^*$ is then given in terms of the solutions $w_{ij}$ of the *cell problems* by

$$A^*_{ijkl} = \int_{Y_0} A(e_{ij} + e(w_{ij})) : (e_{kl} + e(w_{kl}))dy \quad \forall i,j,k,l \in \{1,2\}. \tag{5}$$

Restricting the analysis to periodic composites is an acceptable limitation, as the set of Hooke's laws of periodic composites is dense in the set of all possible Hooke's laws reachable with composites [1]. However, restricting the set

of periodic composites to square cells with rectangular holes is clearly a loss of generality since, for example, the resulting homogenized Hooke's laws are never isotropic (for intermediate densities). Exploring a larger range of periodic microstructures is an obvious line of research for future work.

### 3.3 Sensitivity of the homogenized elasticity tensor

The computation of the sensitivity of the homogenized elasticity tensor with respect to the parameters of the cell design will be based on the notion of shape derivative. We define $W^{1,\infty}_{\#}((0,1)^2;\mathbb{R}^2)$ as the set of $(0,1)^2-$ periodic Lipschitz maps from $(0,1)^2$ with value in $\mathbb{R}^2$ (the # symbol indicates that the functions are $(0,1)^2$-periodic).

**Definition 3.1.** Let $\theta \in W^{1,\infty}_{\#}((0,1)^2;\mathbb{R}^2)$. The shape derivative of a function $F(Y_0)$ is defined as the Frechet derivative in $W^{1,\infty}$ at 0 of the application $\theta \mapsto F((\mathrm{Id}+\theta)Y_0)$

$$F((\mathrm{Id}+\theta)Y_0) = F(Y_0) + \langle F'(Y_0), \theta\rangle + o(\theta) \quad \text{with} \lim_{\theta\to 0} \frac{|o(\theta)|}{\|\theta\|_{W^{1,\infty}_{\#}}} = 0$$

where $F'(Y_0)$ is a continuous linear form on $W^{1,\infty}_{\#}((0,1)^2;\mathbb{R}^2)$.

Let $\mathcal{M}_N$ be the set of squared $N \times N$ matrices and $\mathcal{M}^s_N$ the subset of symmetric ones.

**Lemma 3.1.** *The shape derivative of $A^*_{ijkl}$ is given by:*

$$\begin{aligned}\left\langle (A^*_{ijkl})'(Y_0), \theta \right\rangle &= \int_{Y_0} A(e_{ij}+e(w_{ij})) : (e_{kl}+e(w_{kl}))\,\mathrm{div}(\theta)dy \\ &- \int_{Y_0} A(e_{ij}+e(w_{ij})) : \langle de(w_{kl});\theta\rangle dy \\ &- \int_{Y_0} A(e_{kl}+e(w_{kl})) : \langle de(w_{ij});\theta\rangle dy, \end{aligned} \tag{6}$$

*where $de(w)$ is a linear operator from $W^{1,\infty}_{\#}(Y_0;\mathbb{R}^2)$ to $L^2(Y_0;\mathcal{M}^s_2)$ defined for every $w \in H^1_{\#}(Y_0,\mathbb{R}^2)$ by*

$$\langle de(w),\theta\rangle = \frac{1}{2}(\nabla w \nabla\theta + \nabla\theta^T \nabla w^T).$$

*Proof.* The proof is classical (see e.g. [16]), thus we simply give its main idea. It relies on the Lagrangian method of Cea [9] which amounts to introduce a Lagrangian, defined as the sum of formula (5) for $A^*_{ijkl}$ and of the variational formulation (4). Differentiating with respect to the state variable gives the adjoint system. It turns out that the problem is self-adjoint, so no adjoint appears in (6). Differentiating with respect to the shape leads to the final result. □

## 3.4 Computing the homogenized elasticity tensor

The set of effective elasticity tensors $\{A^*_\alpha(m) | (m, \alpha) \in L^\infty(D, [0,1]^2 \times \mathbb{R})\}$ has to be characterized. The proposed strategy consists in computing the material properties for a discrete sample of parameters values and using the collected data to construct a surrogate model for the constitutive law (by a simple interpolation).

### 3.4.1 Cell orientation

The considered cells $Y_\alpha(m)$ are not isotropic, nor are their corresponding elasticity tensors $A^*_\alpha(m)$. Therefore, their elastic behavior depends on their orientation $\alpha$. Let $R(\alpha)$ a fourth-order tensor defined by :

$$\forall \xi \in \mathcal{M}_2^s \quad R(\alpha)\xi = Q(\alpha)^T \xi Q(\alpha)$$

where $Q(\alpha) \in \mathcal{M}_2$ is the rotation matrix of angle $\alpha$. Then, the dependency of $A^*_\alpha(m)$ with respect to the angle $\alpha$ can be made explicit as follows

$$A^*_\alpha(m) = R(\alpha)^T A^*_0(m) R(\alpha)\,. \tag{7}$$

Unlike the parameters $m = (m_1, m_2)$, the dependency on the orientation $\alpha$ is explicit and the derivative of the elasticity tensor with respect to $\alpha$ is also algebraically known. The numerical computation of the homogenized elasticity tensors $A^*_\alpha(m)$ can thus be restricted to the case $\alpha = 0$. Note that a rotation of the cell by an angle $\pi$ does not change its Hooke's law as $R(\pi) = -\,\mathrm{Id}$. Hence the optimal orientation can only be defined modulo $\pi$.

### 3.4.2 Derivatives of the homogenized elasticity tensor

In order to compute the derivative of the homogenized tensor, with respect to $m_1$ (respectively to $m_2$), we choose a specific deformation field $\theta$ in the shape derivative formula (6). Introducing the smooth $(0,1)^2$-periodic vector fields $\theta_1$ and $\theta_2$, defined by

$$\theta_1 = c_1(\sin(2\pi y_1), 0)^T\ , \quad \theta_2 = c_2(0, \sin(2\pi y_2)^T\ ,$$

where $c_1 = -\sin(\pi m_1)^{-1}, c_2 = -\sin(\pi m_2)^{-1}$ are rescaling coefficients, it is easy to check that $Y_0(m_1 + \delta m_1, m_2 + \delta m_2) = (\mathrm{Id} + \delta m_1 \theta_1 + \delta m_2 \theta_2)(Y_0(m))$, where $(\delta m_1, \delta m_2)$ is a small increment. It follows that, for $i = 1, 2$,

$$\frac{\partial A^*_0}{\partial m_i}(m) = \langle (A^*_0)'(Y_0), \theta_i \rangle\ .$$

Therefore, (6) leads to the sensitivities of $A^*_0(m)$ with respect to $m_1$ and $m_2$.

### 3.4.3 Numerical implementation

The considered cells $Y_0(m)$ have cubic symmetry, thus the corresponding homogenized elasticity tensors $\{A_0^*(m)$ are orthotropic and fully characterized by only four of its entries, namely $(A_0^*(m))_{1111}, (A_0^*(m))_{1122}, (A_0^*(m))_{2222}, (A_0^*(m))_{1212}$. The three cell problems (3) on $Y_0(m)$ are solve using a finite element method. Once the correctors $w_{11}, w_{22}, w_{12}$ are computed, the four independent coefficients of the elasticity tensor are obtained using equation (5). Similarly, the sensitivities to the parameters $m_1$ and $m_2$ are deduced from the integral formula (6).

We discretized the space of the parameter $m$ describing the microstructure on a regular grid with 50 elements in each direction. We then compute numerically the effective elasticity tensors $A_0^*(m)$ for each so-defined samples of parameters $m = (m_1, m_2)$, by using the finite element solver FreeFem++ [13]. We emphasize the fact that rotating a periodic cell by $\pi/2$ while exchanging $m_1$ and $m_2$ leaves it invariant. Thus, the computation of the effective elasticity tensor can be restricted to the samples where $m_1 \leq m_2$.

To interpolate the effective elastic law, we take advantage of the structure of the $P_1$-functions in FreeFem++. Indeed, we have the value of all components of $A^*$ and their sensitivities on each vertex of the discretization grid of $m$, which defines a $P_1$-function. Hence, there is no need to implement a specific interpolation function in FreeFem++ and during the optimization step, the call to the effective elasticity tensor is not time consuming.

We noticed from our numerical results that all the homogenized coefficients of $A^*$ are strictly decreasing, with respect to $m_1$ and $m_2$ (as could be expected from mechanical intuition). This property must be preserved during the interpolation of the elasticity tensor. Among the several interpolation methods that were investigated, namely linear interpolation, splines, Kriging, only the linear interpolation ensures the strict monotonicity of the functions. However, using a linear interpolation, the derivatives of the interpolated tensor with respect to $m_1$ and $m_2$ are piecewise constant and discontinuous. Thus, these derivatives are not very precise and difficult to use in an optimization algorithm. Thus, we decided to interpolate the sensitivities, computed from (6), separately by the same $P_1$ algorithm. This choice makes the values of the homogenized coefficients and their sensitivities slightly inconsistent. However, in practice, the chosen interpolations are precise enough so not to impair the convergence of the gradient type algorithm used during the optimization stage.

### 3.4.4 Degeneracy issues

There exists two kinds of configurations where the $Y_0(m)$ cells are degenerate. Firstly, when one of the microstructure parameters $m_i$ is equal to 0 but, not the other one. The square cell is full of material but features a central crack. Hence, the homogenized tensor $A_0^*(m)$ is not equal to the pure solid tensor $A$. Numerically, the crack is represented by a thin rectangle excluded from the mesh of the cell of width $m_i = 10^{-3}$.

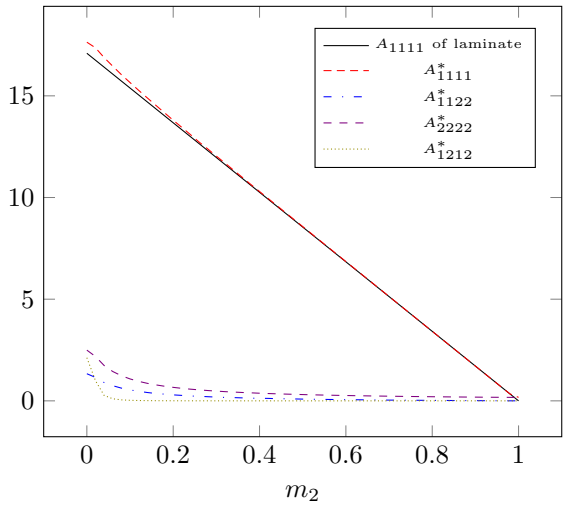


Figure 3: Comparison of the numerically computed components of $A_0^*((1, m_2))$ with the theoretical ones given by the rank-one laminate formula.

Secondly, when one of the microstructure parameters $m_i$ is equal to 1, the domain obtained by periodic repetition of the cell is no longer connected, but is rather a union of disconnected parallel bars. To avoid the degeneracy of the homogenized elasticity tensor in such a case, we impose $m_i$ to be less than a maximal value of $(1 - 10^{-3})$. However, in the case when $m_i$ is close to 1, the composite material is a single lamination along the $y_j$ axis (with $j = 3 - i$) of phase $A$ and void in respective proportions $\rho = 1 - m_j$ and $(1 - \rho) = m_j$. The homogenized elasticity tensor $A_0^*(m)$ is then algebraically known [2]. All of its components are equal to 0, except $(A_0^*(m))_{iiii}$ given by

$$(A_0^*(m))_{iiii} = \frac{4\mu(\lambda + \mu)}{\lambda + 2\mu}\rho$$

The Lamé coefficients of the isotropic material used numerically are : $\lambda = 12.96$ and $\mu = 5.56$, corresponding to a Young modulus $Y = 15$ and to a Poisson ratio $\nu = 0.35$. As shown in Figure 3, the numerical results are close to the theoretical ones of the rank-one laminate. It is therefore a justification of the above approximation which amounts to replace $m_i = 1$ by the smaller value $m_i = (1 - 10^{-3})$ when computing the homogenized tensor.

### 3.5 Numerical results and discussion

Numerical results for the entries of the homogenized tensor $A^*$ and their derivatives as functions of the parameters $m$ are displayed on Figure 4. The results are consistent, since the gradients are orthogonal to the isolines. When the cell is full and without crack, i.e. $m = 0$, the homogenized tensor $A_0^*(m)$ is equal to $A$.

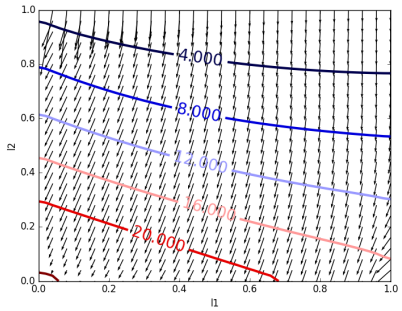


(a) $(A_0^*(m))_{1111}$, with $A_{1111} = 24.07$

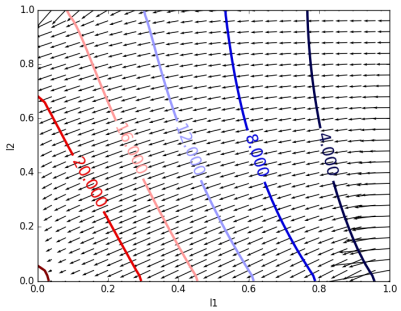


(b) $(A_0^*(m))_{2222}$, with $A_{2222} = 24.07$

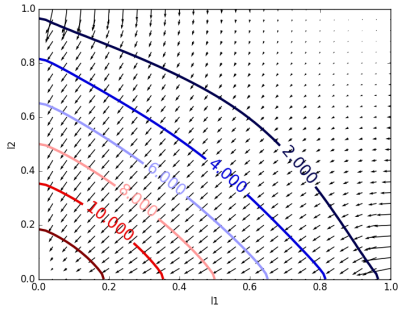


(c) $(A_0^*(m))_{1122}$, with $A_{1122} = 12.96$

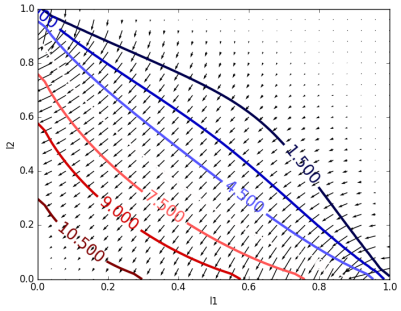


(d) $(A_0^*(m))_{1212}$, with $A_{1212} = 11.11$

Figure 4: Isolines of the entries of the homogenized tensor $A^*$ and their gradient (small arrows) according to the parameters $m$. The $x$-axis is $m_1$, the $y$-axis is $m_2$

When the cell is close to be empty, i.e. $m$ close to $(1,1)$, the homogenized tensor is converging to the null tensor. Moreover, one can easily check, that the entries of $A_0^*(m)$ decrease, when $m_1$ is fixed and $m_2$ is increasing (and vice versa). In other words, the cell is globally weaker when its hole is widening in one direction or the other. However, the sensitivity of the component $(A_0^*(m))_{1111}$ to the parameter $m_2$ is greater than the one to the parameter $m_1$, see Figure 4(a). That is explained by the fact that, along the $y_1$ axis, the strength of the cell is mainly insured by the material in the areas above and below the hole, whose sizes depend on $m_2$. As could be expected, the homogenized elasticity tensor is quite smooth with respect to the parameter $m$, so it is amenable to a gradient based optimization method.

# 4 Processing: optimization among the set of periodic composite materials

## 4.1 Settings of the homogenized problem

In this paper, we focus on the compliance minimization problem, hence the cost function $J$ defined in Section 2 is given by

$$J(\Omega) = \int_{\Gamma_N} g \cdot u \, ds,$$

whose relaxed version for composite material reads as

$$J^*(\theta, A^*) = \int_{\Gamma_N} g \cdot u^* \, ds,$$

which is also equal to

$$J^*(\theta, A^*) = \min_{\tau \in H_0} \int_D A^{*-1}\tau : \tau \, \mathrm{dx},$$

where

$$H_0 = \left\{ \tau \in L^2(D; \mathcal{M}_2^s) \text{ such that } \begin{array}{l} \mathrm{div}(\tau) = 0 \text{ in } D \\ \tau n = g \text{ on } \Gamma_N \\ \tau n = 0 \text{ on } \Gamma \end{array} \right\}.$$

Note that the results of the present section are not restricted to compliance minimization. For other objective functions or multiple load problems, we refer to [10].

The optimization problem defined in Section 2 can be recast as a minimization problem over the stress field and the admissible microstructures [1]. Namely, it is equivalent to

$$\inf_{\substack{\sigma \in H_0 \\ m \in L^\infty(D;[0,1]^2) \\ \alpha \in L^\infty(D;\mathbb{R}) \\ \int_D \theta(m) \, \mathrm{dx} \leq V}} \int_D A_\alpha^{*-1}(m)\sigma : \sigma \, \mathrm{dx},$$

where

$$\theta(m) = 1 - m_1 m_2$$

is the local density of the periodic microstructure of parameters $m$.

In order to solve this problem, we use an alternate minimization algorithm [3], minimizing successively with respect to the stress field $\sigma$, the microstructure $m$ and the orientation $\alpha$ of the cell. We introduce the corresponding Lagrangian

$$\mathcal{L}(m, \alpha, \sigma, \ell) = \int_D A_\alpha^{*-1}(m)\sigma : \sigma \ \mathrm{dx} + \ell \left( \int_D \theta(m) \ \mathrm{dx} - V \right),$$

where $\ell$ is the Lagrange multiplier associated to the volume constraint.

**Minimization w.r.t the stress field.** For given design fields $(m, \alpha)$, the minimization with respect to the stress field $\sigma$ amounts to solve the elasticity problem with a material of elasticity tensor equal to $A_\alpha^*(m)$ in $D$.

**Minimization w.r.t the microstructure $m$.** For a given stress field $\sigma$, to minimize with respect to the microstructure $m$, we use the projected gradient algorithm. Recall that the considered problem is self-adjoint. The descent directions are given by the derivatives of $\mathcal{L}$ with respect to $m$

$$\left\langle \frac{\partial \mathcal{L}}{\partial m_i}(m, \alpha, \sigma, \ell), h \right\rangle = - \int_D \left( \frac{\partial A_\alpha^*}{\partial m_i}(m) A_\alpha^{*-1}(m)\sigma : A_\alpha^{*-1}(m)\sigma + \ell m_j \right) h \ \mathrm{dx},$$

with $j = 3 - i$. We have to select a descent direction $h = dm_i$ such that

$$\left\langle \frac{\partial \mathcal{L}}{\partial m_i}(m, \alpha, \sigma, \ell), dm_i \right\rangle < 0,$$

which is achieved by choosing

$$dm_i = \frac{\partial A_\alpha^*}{\partial m_i}(m) A_\alpha^{*-1}(m)\sigma : A_\alpha^{*-1}(m)\sigma + \ell m_j \quad \text{in } D. \tag{8}$$

The update of the microstructure at iteration $n$ is given by :

$$m_i^{n+1} = P_{[0,1]}(m_i^n + \mu_m dm_i) \tag{9}$$

where $\mu_m > 0$ is the step size and $P_{[0,1]}$ is the projection operator on the interval $[0, 1]$. The value of $\ell$ is updated at each iteration by a dichotomy process designed to respect the volume constraint.

**Minimization w.r.t the orientation $\alpha$.** To minimize with respect to the orientation, we could use the same method as for the minimization with respect to the microstructure, but there exists a better (more efficient) algorithm than the gradient descent method to compute the optimal orientation. Pedersen [20] proved that the optimal orientation of an orthotropic cell for a given displacement field is the one where the cell is aligned with the principal directions of

the strain tensor. A similar result with a given stress field can easily be shown in the same way.

First, the principal (orthogonal) directions of the given stress field $\sigma$ are computed. According to Pedersen formulas, we have to align the principal directions $\sigma$ with the orientation of the cell. Hence, at this stage, the optimal orientation is known up to an additive multiple of $\frac{\pi}{2}$. However, by choosing to align the vector $a_1 = (\cos(\alpha), \sin(\alpha))$ with the eigenvector of $\sigma$ of smallest eigenvalue (possibly negative), the angle $\alpha$ is defined modulo $\pi$. Note that the cases where $\sigma$ is proportional to the identity are generically limited to isolated points (and thus the set of such point is of null measure). This approach is more efficient than the gradient descent method, mainly because it is a global minimization method, providing an optimal orientation at each iteration. However, this method can usually not be generalized to other objective functions.

**Remark 1.** *For multiple loads cases, Pedersen algorithm does not work. However, the optimal orientation at one point still only depends on the values of the local stress fields and is solution of a one dimensional minimization problem. Thus the global minimization of the cost function with respect to the orientation $\alpha$ remains relatively easy even without any explicit expression.*

## 4.2 Implementation

**Complete optimization algorithm.** The optimization algorithm is an iterative method, structured as follows :

1. Initialization of the design parameters $(m, \alpha)$, for example we take $m_1 = m_2$, constant satisfying the volume constraint, and $\alpha = 0$.
2. Iteration until convergence, for $n \geq 0$ :
   (a) Computation of $\sigma^n$ through a problem of linear elasticity with $A^*_{\alpha^n}(m^n)$ as elasticity tensor
   (b) Updating the orientation $\alpha^{n+1}$, using the Pedersen formulas
   (c) Updating the design parameters $m^{n+1}$, using (8-9), with the parameters $\sigma^n$ and $\alpha^n$.

We implemented the topology optimization in the finite element software FreeFem++ [13] (see [4] for the use of FreeFem++ in optimal design). All unknowns are discretized using $P_1$-functions.

**Stress field $\sigma$.** We solve the elasticity problem, namely we compute the displacement field

$$u \in V_D := \{v \in H^1(D; \mathbb{R}^2) \text{ such that } v = 0 \text{ on } \Gamma_D\},$$

such that, for all $v \in V_D$,

$$\int_D A^*_0(m) R(\alpha)^T e(u) : R(\alpha)^T e(v) \, \mathrm{dx} = \int_{\Gamma_N} g \cdot v \, \mathrm{ds} \, .$$

We use $P_1$ finite elements to compute the displacement $u$. Afterwards, the stress tensor $\sigma$ is obtained as the interpolation of the $P_0$-function $R(\alpha)A_0^*(m)R(\alpha)^T e(u)$ in the set of $P_1$ finite elements

**Minimization with respect to the orientation.** As recalled previously, the minimizer of $\mathcal{L}(m,\alpha,\ell,\sigma)$ with respect to $\alpha$ is reached when the cell is aligned with the eigenvectors of the stress tensor $\sigma$. Denote by $a$ and $b$ the rotation matrices of angles $\alpha$ and $2\alpha$, respectively,

$$a = Q(\alpha)\,, \quad b = Q(2\alpha)\,. \tag{10}$$

As is well known [20], the Hooke's law depends on the orientation $\alpha$ only through the tensor $R(\alpha)$ which, in turns, only depends on the rotation matrix $b$. If we choose the first column $a_1$ to be aligned with the eigenvector of $\sigma$ of smallest eigenvalue, we get that

$$b_1 = \frac{1}{\sqrt{(\sigma_{11}-\sigma_{22})^2 + 4\sigma_{12}^2}}(\sigma_{11}-\sigma_{22}, 2\sigma_{12})^T\,.$$

**Remark 2.** *In practice, Voigt notations are used, in order to replace tensors product by matrix product. Hence, a second-order tensor $\xi$ is represented by the following vector :*

$$\{\xi\} = \left(\xi_{11}, \xi_{22}, \frac{\xi_{12}+\xi_{21}}{\sqrt{2}}\right)^T\,.$$

*And the fourth-order tensor $R(\alpha)$ can be represented by a matrix, which is expressed only using the vector $b_1 = (b_{11}, b_{21})$*

$$\{R(\alpha)\} = \begin{pmatrix} \frac{1+b_{11}}{2} & \frac{1-b_{11}}{2} & -\frac{b_{21}}{\sqrt{2}} \\ \frac{1-b_{11}}{2} & \frac{1+b_{11}}{2} & \frac{b_{21}}{\sqrt{2}} \\ \frac{b_{21}}{\sqrt{2}} & -\frac{b_{21}}{\sqrt{2}} & b_{11} \end{pmatrix}. \tag{11}$$

**Minimization with respect to the cell parameters $m$.** At each iteration, the descent directions for both parameters $m_1$ and $m_2$ are computed using (8). Numerically, the fields $m_1$ and $m_2$ are $P_1$-functions. Thus, the partial derivatives for the Lagrangian, denoted by $\frac{\partial \mathcal{L}}{\partial m_i}$ are interpolated, using a $H^1$ equivalent norm, by solving the following variational formulation : $\forall h \in H^1(D,\mathbb{R})$

$$\int_D \left(\frac{\partial \mathcal{L}}{\partial m_i} h + \eta^2 \nabla \frac{\partial \mathcal{L}}{\partial m_i} \cdot \nabla h\right) \mathrm{dx} = -\int_D \left(\frac{\partial A_0^*}{\partial m_i}(m) R(\alpha)^T e(u) : R(\alpha)^T e(u) + \ell m_j\right) h \ \mathrm{dx}$$

with $\eta > 0$ a small coefficient, which typically depends on the size of the elements of the mesh. The purpose of this small coefficient is to numerically regularize the partial derivatives on a lengthscale of order $\eta$ and to limit the checkerboard effect [21]. The update of the fields is then given by

$$m_i^{n+1} = \max\left(0, \min\left(1, m_i^n - \mu_m \frac{\partial \mathcal{L}}{\partial m_i}\right)\right).$$

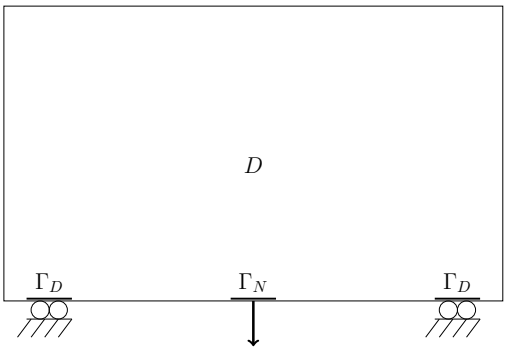


Figure 5: Boundary conditions for the bridge problem

In practice, we use an adaptative step size $\mu_m$. At each iteration, if the newly computed homogenized structure is accepted (i.e. if its compliance is lower than the one of the previous structure), the step size $\mu_m$ is increased of 20%. On the contrary, if the newly computed structure is rejected, the step size is divided by 2.

The Lagrange multiplier $\ell$ is computed so that the volume constraint

$$\int_D \theta(m) = V$$

is satisfied almost exactly. To this end, we use a dichotomy process (note that the variational formulation that defines $\partial\mathcal{L}/\partial m_i$ has not to be solved at each iteration of the dichotomy, as the dependency on $\ell$ is linear).

### 4.3 Numerical results and discussion

We have numerically implemented the optimization algorithm for the bridge problem, see Figure 5 for the boundary conditions. The domain size is $22 \times 13$ and it is discretized by a structured triangular mesh. Taking 4 nodes per unit length on the boundary yields a mesh with 18304 triangles and 9293 vertices. The volume constraint is fixed to 30% of the working domain. The algorithm converged quickly and smoothly, see Figure 6. The results are displayed on Figure 7. The optimized design parameters $m_1$ and $m_2$ in Figures 7(c) and 7(d) are most of the time not equal (when they are different from the extreme values 0 and 1), and the optimized orientation (Figure 7(b)) is almost radial. This is a clear manifestation that the obtained optimal composite is anisotropic.

The minimal compliance for a single-load case is known to be reached by rank-2 laminates [1]. We have also computed the optimal design for such laminates. The results are displayed in Figure 8 (note that the $m_1$ and $m_2$ parameters have a different signification for rank-2 laminates). The two optimized designs, respectively with square cells and laminates, are closed to each other. Indeed, both feature a radial structure, with high density on the main arch and

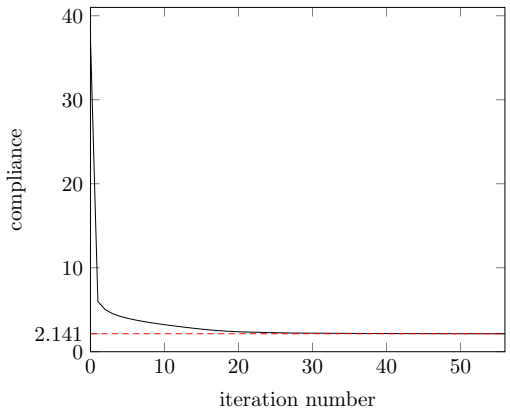


Figure 6: Convergence history of the objective function (compliance) for the bridge

in the loading areas. Moreover, the final compliance 2.141 for the locally periodic square cells case is closed to the optimal one 2.100 for rank-2 laminates: the difference is less than 2%. This can be seen as a justification of our choice of such cells. For the sake of comparison, the same test case has been performed with the Solid Isotropic Material with Penalization (SIMP) method: the elastic law is represented as a power law of the density (the maximal exponent is 3). The optimal compliance obtained by this method is equal to 2.38, which is 11% greater than the final compliance reached by the homogenization method. The discretized mesh was the same than the one for the homogenization method. In order to obtain a mesh independent design (and to avoid checkerboards), a sensitivity filter was applied. The radius of the filter was equal to three mesh-element sizes. The optimal design is displayed on Figure 9(b). The optimal design without penalization (i.e. with exponent 1) was also computed and, of course, displays large grey areas, see Figure 9(a). Its compliance is equal to 1.99, a much lower value than that for the homogenization method, as it is expected [1], since the SIMP method (with exponent 1) is equivalent to use fictitious isotropic material which do not fit into the Hashin-Shtrikman bounds. Hence, the optimized compliance is much lower than the previous ones, including the compliance reached by the rank-2 laminates which is the global optimum.

We also ran several tests with additional constraints on the design parameters, denoted by B, C, D and E. The previous one is denoted by A. The test cases and the results are summarized in Table 1, sorted according to the final compliance. The lower compliance is reached when we optimize with respect to the three variables, $m_1$, $m_2$ and $\alpha$. In this case, the set of admissible shapes is the largest and contains all other used subsets.

When the orientation of the cells is fixed to zero (cases B and D, see Figures 10 and 11), the anisotropy of the cells is no longer an asset. The optimized design is then self-penalized. Only small areas of intermediate density are visible. Most

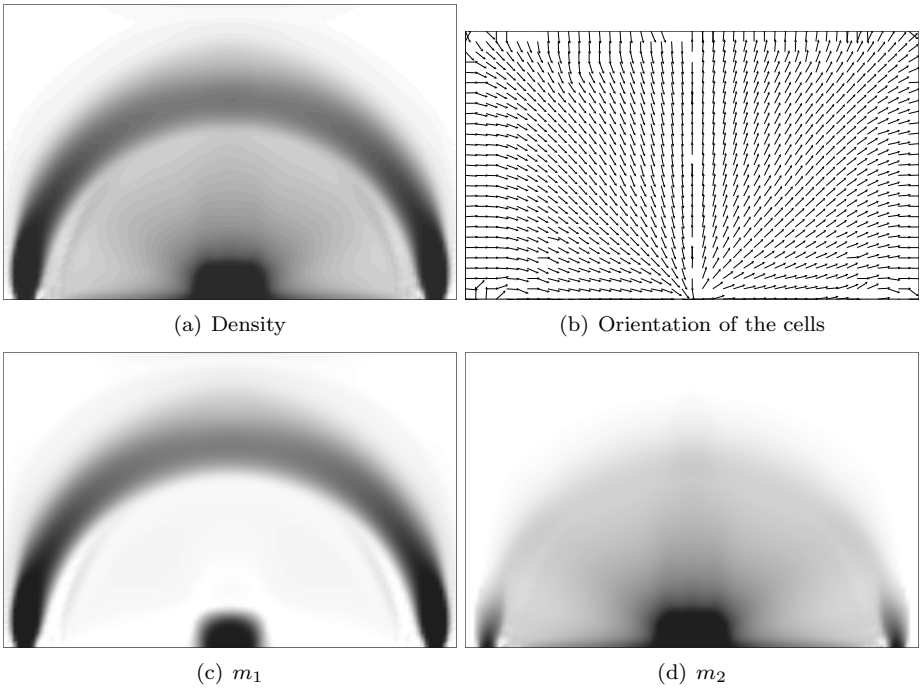

(a) Density (b) Orientation of the cells

(c) $m_1$ (d) $m_2$

Figure 7: Optimized design of the bridge, case A : no constraint on the design variables.

| Case | Constraint on $m$ | Constraint on $\alpha$ | Optimal compliance |
|---|---|---|---|
| A | none | none | 2.141 |
| B | none | $\alpha = 0$ | 2.524 |
| C | $m_1 = m_2$ | none | 2.549 |
| D | $m_1 = m_2$ | $\alpha = 0$ | 2.600 |
| E | $m_1 = m_2 = \sqrt{0.7}$ | none | 5.121 |
| reference | $m_1 = m_2 = \sqrt{0.7}$ | $\alpha = 0$ | 37.410 |

Table 1: Test Cases

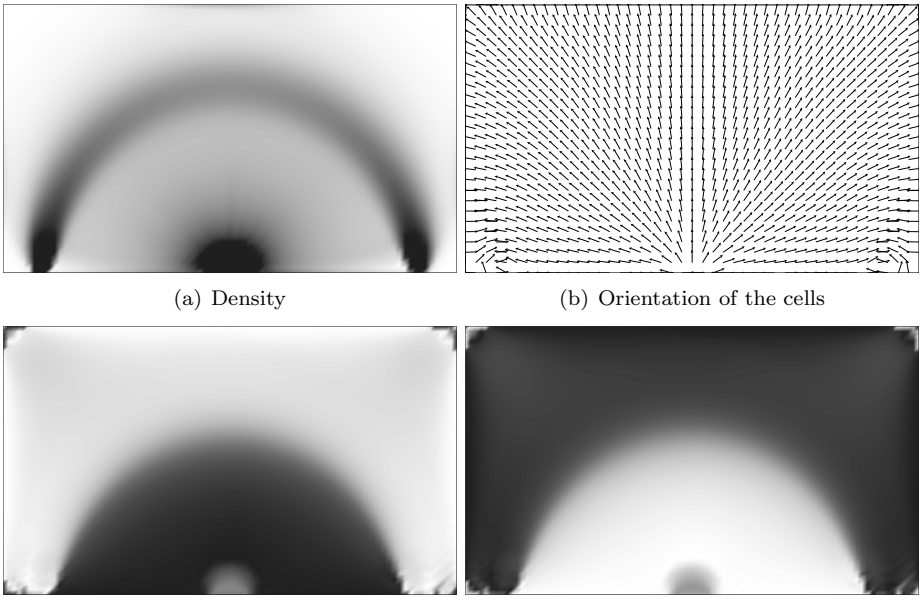

(a) Density (b) Orientation of the cells

(c) $m_1$ (d) $m_2$

Figure 8: Optimized design of the bridge with rank-2 laminates

(a) Density (b) Density

Figure 9: Optimized design of the bridge with penalized (a) and non penalized (b) SIMP method

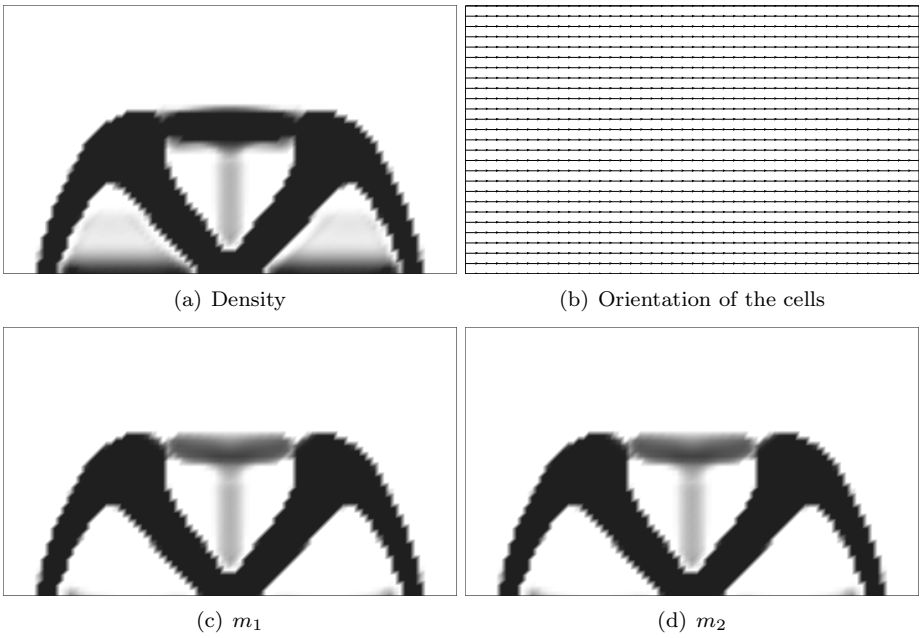

(a) Density (b) Orientation of the cells

(c) $m_1$ (d) $m_2$

Figure 10: Optimized design of the bridge, case B : $\alpha = 0$.

of the domain is either made of void or plain material. Indeed the best strategy to bear stress, when the cell is not aligned with the principal directions of $\sigma$, is to be strong in all directions, and so to be isotropic.

When the dimensions of the holes are fixed (case E), the optimal orientation of Pedersen is still valid. The optimized orientation is closed to the one of case A. However, the optimized compliance is much greater. Nevertheless, the compliance is decreased by 87% compared to the reference value.

# 5 Post-Processing : projection of the optimized microstructure

The last step is to construct a sequence of classical or genuine shapes that actually converges toward the computed optimal composite. This sequence is indexed by a small positive parameter $\varepsilon > 0$ which is the size of the period of the periodic composite. In numerical practice, one has to choose a specific value of $\varepsilon$ and then the projection will be done for this chosen periodicity. Of course, the smaller $\varepsilon$, the more detailed will be the resulting genuine shape.

In section 5.1 we define a set of sequences of shapes that converge toward square periodic composites. Each sequence of shapes is defined by the microstructure $m$ of the composite and a mapping function $\varphi$. As shown in section 5.2 each reachable square periodic composite has to be build on a conformal lattice.

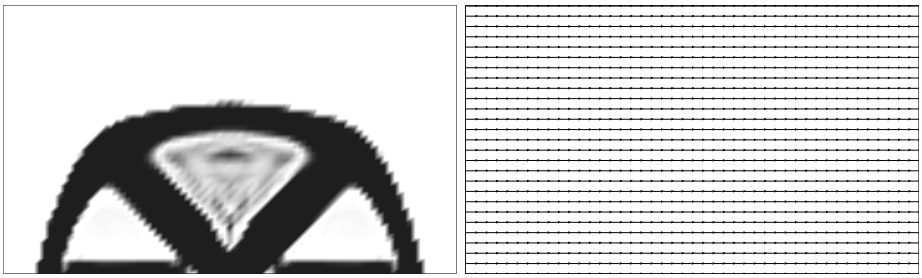

(a) Density (b) Orientation of the cells

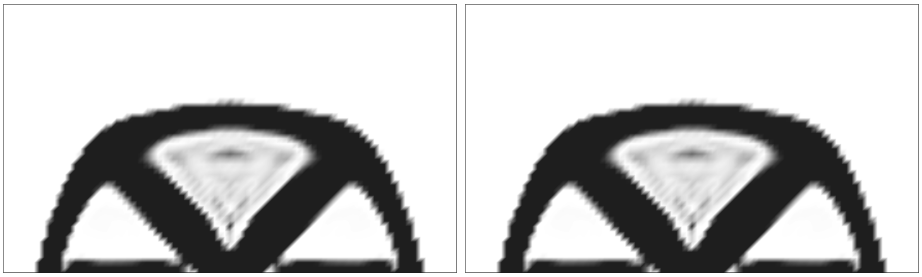

(c) $m_1$ (d) $m_2$

Figure 11: Optimized design of the bridge, case D : $m_1 = m_2$ and $\alpha = 0$.

Equivalently, the Laplacian of the orientation of the cells has to be a harmonic function. This condition is enforced to the optimal composite by pursuing the optimization while imposing this extra constraint (section 5.3). It remains to compute the mapping function $\varphi$ to completely define a sequence of genuine shapes converging toward the optimum obtained. To be able to cope with the fact that the orientation if defined up to a rotation of angle $\pi$, we introduce an abstract manifold on which the mapping function is defined (section 5.4). Its computation then reduced itself to solve two linear problems (section 5.5).

## 5.1 Sequences of shapes

**Projection of the optimized design, case without optimal orientation.** First, we consider the case where the orientation of the cell is constant in the whole domain $D$. Our unit cells (rectangular hole in a square) can be analytically defined by

$$Y_0(m) = \Big\{ y \in [0,1]^2 \text{ such that } \cos(2\pi y_1) \geq \cos(\pi(1-m_1)) \\ \text{or } \cos(2\pi y_2) \geq \cos(\pi(1-m_2)) \Big\}.$$

Hence, to build a cellular structure $\Omega_\varepsilon(m)$, we have to pave the domain $D$ with cells $\varepsilon Y_0(m)$. However, the hole size $m$ is varying inside $D$ so the periodicity

cell is macroscopically modulated, as is classical in homogenization. Thus the genuine shape $\Omega_\varepsilon(m)$ is defined by

$$\Omega_\varepsilon(m) = \Big\{ x \in D \text{ such that } \cos\left(2\pi\frac{x_1}{\varepsilon}\right) \geq \cos(\pi(1-m_1(x)) \\ \text{or } \cos\left(2\pi\frac{x_2}{\varepsilon}\right) \geq \cos(\pi(1-m_2(x)\Big\},$$

where $m_1(x), m_2(x)$ are functions defined on $D$ with values in $[0,1]$. The values of $m_1$ and $m_2$ are not necessarily constant in each cell of the structure. Hence, the cellular structure $\Omega_\varepsilon(m)$ do not exactly feature square cells with rectangular holes. But, since the size $\varepsilon$ is going to 0, if the functions $m_1$ and $m_2$ are continuous, the sequence of cellular structures is converging to the the composite of local Hooke's law equal to $A_0^*(m)$.
An other approach is to compute on each cell, the mean value of the dimensions parameter $m_1$ and $m_2$ on the cell [22]. With this method, each shape of the minimization sequence is composed of square cells as defined previously. However, its implementation can be time-consuming : for each shape of the sequence, we have to determine each cell of the lattice and its dimension parameters before constructing the final design. Hence, in the following, we will use the previous formulation.

The cellular structures can be defined using level-sets. We introduce two level-set functions $f_{\varepsilon,i}^m \in \mathcal{C}(D;\mathbb{R})$, one for each direction

$$f_{\varepsilon,i}^m(x) = -\cos\left(\frac{2\pi x_i}{\varepsilon}\right) + \cos(\pi(1-m_i(x))).$$

and the level set function

$$F_\varepsilon^m = \min(f_{\varepsilon,1}^m, f_{\varepsilon,2}^m).$$

The final structure $\Omega_\varepsilon(m)$ is then defined by

$$\Omega_\varepsilon(m) = \{x \in D \text{ such that } F_\varepsilon^m(x) \leq 0\}.$$

The construction of a minimizing sequence is immediate : we just have to update the size $\varepsilon$ in the previous level set function.

**Projection of the optimized design, case with optimized orientation.** The crucial point is to take into account the optimized orientation of the cell. Indeed, neither gap nor overlap is allowed between two cells. Hence, cells have to be slightly deformed to ensure the connectivity of the final structure. A map $\varphi = (\varphi_1, \varphi_2)$ from $D$ into $\mathbb{R}^2$ is introduced for this purpose : the inverse of this map distorts a regular grid of squares in order to orientate each square at the optimized orientation $\alpha$. Then, the previous projection method can be applied on this new grid. The final shape, now denoted $\Omega_\varepsilon(\varphi, m)$, is still defined by a

level set function, the same as previously except that the coordinates are now given by the map function $\varphi$:

$$f_{\varepsilon,i}^{\varphi,m}(x) = -\cos\left(\frac{2\pi\varphi_i(x)}{\varepsilon}\right) + \cos(\pi(1-m_i(x)). \tag{12}$$

$$F_{\varepsilon}^{\varphi,m} = \min(f_{\varepsilon,1}^{\varphi,m}, f_{\varepsilon,2}^{\varphi,m}). \tag{13}$$

$$\Omega_{\varepsilon}(\varphi, m) = \{x \in D \text{ such that } F_{\varepsilon}^{\varphi,m}(x) \leq 0\}. \tag{14}$$

**Remark 3.** *The map $\varphi$ is introduced in order to take into account the optimal orientation of the cell. Hence, $\varphi$ depends only on the angle field $\alpha$. In particular, $\varphi$ does not depend on the size $\varepsilon$ of the cells. Once $\varphi$ has been computed, it could be used for any value of this scale parameter.*

## 5.2 Conformality condition

As seen above, we introduce here a map $\varphi$ in order to construct a minimizing sequence of genuine shapes that converges to the optimal composite. We emphasize that the cells featured in those genuine shapes have to converge to square cells, in order that their effective elasticity tensor converges to $A^*$. To perform this, we require that $\varphi$ locally preserves all angles: it is a conformal map. In other words, a small square cell is deformed by $\varphi$ into another almost square cell since the angles between the cell sides, and their diagonals too, are unchanged. This conformality requirement is not specific to square cells. It should be imposed to other types of periodicity cells, like hexagonal cells, in order that the minimizing sequence of genuine shapes converges to the optimal composite $A^*$.

To respect the local orientation, the gradient of $\varphi$ has to be aligned with the axis of the cell given by $a = Q(\alpha)$. Moreover, the proportions of the cell have to be preserved in order to converge to a true square and not simply to a rectangle: $|\nabla\varphi_1| = |\nabla\varphi_2| = e^r$, where $r \in H^1(D)$ is a (scalar) dilation field. The exponential form has been chosen in order to simplify the following equation, and to impose easily the condition of positiveness. Hence,

$$\nabla\varphi = e^r Q(\alpha). \tag{15}$$

It is a classical result that, provided the rotation field is regular, the existence of a compatible conformal mapping $\varphi$ is equivalent to the harmonicity of the orientation $\alpha$. We recall the proof of this result which holds true only in two space dimensions.

**Lemma 5.1.** *Let $\alpha$ be a regular orientation field and $D$ be a simply connected domain. There exists a mapping function $\varphi$ and a dilatation field $r$ satisfying (15) if and only if*

$$\Delta\alpha = 0 \text{ in } D. \tag{16}$$

*Proof.* Recall that in 2-d the rotational or curl of a vector field $u = (u_1, u_2)$ is defined as $\operatorname{curl} u = \nabla \wedge u = \frac{\partial u_2}{\partial x_1} - \frac{\partial u_1}{\partial x_2}$, where $\wedge$ is the 2-d cross product of vectors. Of course, the rotational of a gradient vanishes. Conversely, as $D$ is assumed to be simply connected, a vector-valued map is a gradient if and only if its rotational vanishes. Therefore, there exists a map $\varphi$ which verifies (15) if and only if the rotational of the right hand side vanishes, namely $\operatorname{curl} e^r Q(\alpha)$. Recall from (10) that $a = Q(\alpha)$ with columns $a_1, a_2$. Therefore

$$\operatorname{curl}\left(e^r Q(\alpha)\right) = 0 \Leftrightarrow \forall i \in \{1,2\}, \quad \nabla r \wedge a_i = -\nabla \wedge a_i.$$

Since $(a_1, a_2)$ is an orthonormal basis, $\nabla r$ can be rewritten as

$$\nabla r = (-\nabla \wedge a_2) a_1 + (\nabla \wedge a_1) a_2. \tag{17}$$

We compute

$$\nabla \wedge a_1 = \frac{\partial \alpha}{\partial x_1} \cos(\alpha) + \frac{\partial \alpha}{\partial x_2} \sin(\alpha) \text{ and } \nabla \wedge a_2 = -\frac{\partial \alpha}{\partial x_1} \sin(\alpha) + \frac{\partial \alpha}{\partial x_2} \cos(\alpha). \tag{18}$$

Coupling equations (17) and (18) leads to

$$\nabla r = \left( -\frac{\partial \alpha}{\partial x_2}, \frac{\partial \alpha}{\partial x_1} \right)^T. \tag{19}$$

Finally, the dilation factor $r$ does exist if and only if, the left hand side of (19) is curl free, which leads to the harmonic condition (16) on the orientation field $\alpha$.

□

## 5.3 Optimization over feasible locally square periodic composites

The orientation $\alpha$ given by the optimization does not necessarily respect the conformality condition. In order to enforce this condition, we pursue the optimization algorithm while imposing the harmonicity of $\alpha$. The only step that differs from the optimization algorithm of section 4 concerns the minimization with respect to $\alpha$. We can no longer simply align the periodicity cells with the principal directions of the stress as it leads to solutions that does not satisfy the conformality condition. Moreover, we slightly change the cost function by adding a small regularization term on the orientation. Thus, the optimization with respect to the orientation reduces to the minimization of

$$\int_D \left( A^*_\alpha(m)^{-1} \sigma : \sigma + \eta^2 |\nabla \alpha|^2 \right) \mathrm{dx},$$

under the constraint

$$\int_D \nabla \alpha \cdot \nabla q \, \mathrm{dx} = 0 \text{ for all } q \in H^1_0(D).$$

**Remark 4.** *The regularization term in the above minimization problem is the usual $L^2$-norm of the angle gradient. Other choices are possible, including more "local" criteria. For example, one could replace this gradient norm by a least square difference between the angle and its filtered version, obtained by a local convolution. We did not try this idea since the gradient norm works nicely. Note that the conformality constraint is already nonlocal and thus the additional computational cost of minimizing the gradient norm is somehow negligible.*

We recall that the dependence of the Hooke's law with respect to the orientation is explicitly known by (7). Moreover, the tensor $R(\alpha)$ depends only on $b_1$, see (11), where

$$(b_1, b_2) = b = a^2 = Q(\alpha)^2 = Q(\beta),$$

with $\beta = 2\alpha$ or equivalently

$$b_1 = (\cos(\beta), \sin(\beta)). \tag{20}$$

Let $S(b_1) = R(\alpha)$. As shown by formula (11), $S(b_1)$ is an affine function of $b_1$. Since (7) can be rewritten as

$$A^*_\alpha(m) = S(b_1)^T A^*_0(m) S(b_1),$$

we are left with the minimization problem of

$$\int_D \left( A^*_0(m)^{-1} S(b_1)\sigma : S(b_1)\sigma + \eta^2 |\nabla\beta|^2 \right) \, \mathrm{dx}$$

under the constraints (20) (relating $b_1$ and $\beta$) and

$$\int_D \nabla\beta \cdot \nabla q \, \mathrm{dx} = 0, \text{ for all } q \in H^1_0(D).$$

This minimization problem can not be solved exactly because of the non linear constraint (20). At each iteration $n$, we approximate this constraint by its linearization around the current state. We compute $\delta b_1^n$ and $\delta\beta^n$ that minimizes

$$\int_D A^*_0(m)^{-1} S(b_1^n + \delta b_1)\sigma : S(b_1^n + \delta b_1)\sigma \, \mathrm{dx} + \eta^2 \int_D |\nabla(\beta^n + \delta\beta)|^2 \, \mathrm{dx}$$

under the constraint

$$\int_D \nabla(\beta^n + \delta\beta) \cdot \nabla q \, \mathrm{dx} = 0, \text{ for all } q \in H^1_0(D)$$

and the linearized constraint

$$\delta b_1 = (-\sin(\beta^n), \cos(\beta^n))\delta\beta.$$

Note that, we have

$$\nabla\beta^n = b_1^n \wedge \nabla b_1^n,$$

and thanks to the linearized constraint,

$$\nabla\delta\beta = b_1^n \wedge \nabla\delta b_1.$$

Thus, we can rewrite the linearized minimization problem solely as the variational problem consisting in finding $\delta b_1^n \in H^1(D;\mathbb{R}^2)$ and $p^{n+1} \in H_0^1(D)$ such that for all test functions $\delta c \in H^1(D;\mathbb{R}^2)$ and $q \in H_0^1(D)$,

$$2\int_D A_0^*(m)^{-1} S(b_1^n+\delta b_1^n)\sigma : S'(\delta c)\sigma \ \mathrm{dx} + 2\eta^2 \int_D (b_1^n \wedge \nabla(b_1^n+\delta b_1^n))\cdot(b_1^n \wedge \nabla\delta c) \ \mathrm{dx} + \int_D (b_1^n \wedge \nabla\delta c)\cdot\nabla p^{n+1} \ \mathrm{dx} = 0 \quad (21)$$

and

$$\int_D (b_1^n \wedge \nabla(b_1^n + \delta b_1^n))\cdot\nabla q \ \mathrm{dx} = 0. \quad (22)$$

In (21), $p^{n+1}$ is the Lagrange multiplier, corresponding to the constraint (22) and $S'(\delta c)$ is the directional derivative of $S(b_1)$ in the direction $\delta c$. Recall that $S$ is affine so $S'$ is easy to determine.

The vector field $b_1$ is then updated after renormalization of $b_1^n + \delta b_1^n$

$$b_1^{n+1} = \frac{b_1^n + \delta b_1^n}{|b_1^n + \delta b_1^n|}. \quad (23)$$

**Regularization algorithm.** The above algorithm is structured as follows :

1. Initialization of the design parameters $(m, b)$ with the results of the optimization without the conformality constraint.
2. Iteration until convergence, for $n \geq 0$ :
   (a) Computation of the strain tensor $e(u^n)$ through the problem of linear elasticity.
   (b) Computation of the increment $\delta b_1^n$ by solving the variational problem (21,22).
   (c) Updating of the orientation with (23).
   (d) Updating of the design parameters $m^n$, using (8,9), with the parameters $b^n$, where the Lagrange multiplier $\ell$ for the volume constraint in (8) is again computed by dichotomy.

**Numerical Results.** We implemented this algorithm for the optimized bridge (case A). Regularized orientation is displayed in Figure 12 and a comparison between the optimized orientation and the regularized orientation is displayed in Figure 13. There is no significant difference concerning the dimension parameters $m$. Hence they are not produced here.

The regularized orientation is not far from the optimized one. The regularization occurred mainly in areas where density is closed to 0 or to 1, i.e.

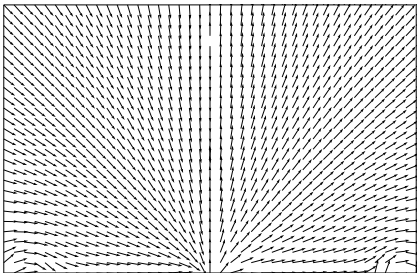

Figure 12: Regularized Orientation for the bridge case

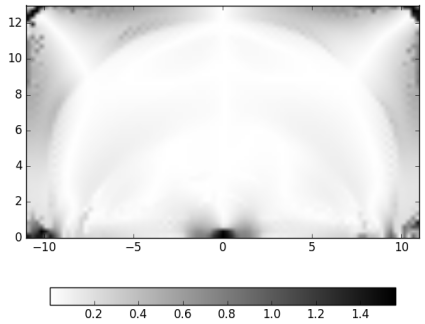


Figure 13: Angle difference in radian between the optimized orientation and the regularized orientation for the bridge case

where the homogenized material is almost isotropic and the orientation has no significant impact on the Hooke's law. Moreover, the singularity at the point $(0,0)$ is put outside of the working domain $D$ by the regularization algorithm. This is crucial to compute the mapping $\varphi$, but does not really degrade the final design since in the vicinity of the singularities the density is equal to 1. The compliance of the regularized structure is equal to 2.169, to be compared with the value 2.141 for case A: the degradation of the solution is lower than 2%.

### 5.4 Reconstruction of a sequence of shapes

Once the optimal locally square periodic composite that satisfies the conformality condition has been computed, it remains to determine the corresponding grid map $\varphi$ from $D$ into $\mathbb{R}^2$, that satisfies (15). As shown in the proof of Lemma 5.1, the dilation field $r$ of the cells is given by

$$\nabla r = (\nabla \wedge a_1)a_2 - (\nabla \wedge a_2)a_1.$$

Thus, it can be computed simply by minimizing

$$\int_D |\nabla r - (\nabla \wedge a_1)a_2 + (\nabla \wedge a_2)a_1|^2 \ \mathrm{dx} \tag{24}$$

over the maps $r \in H^1(D)$. If the orientation $\alpha$ is coherent on the working domain $D$, the computation of $\varphi$ reduced to the minimization of

$$\int_D |\nabla \varphi - e^r a|^2 \, dx$$

over the fields $\varphi \in H^1(D;\mathbb{R}^2)$. Unfortunately, as a consequence of the property of central symmetry of the periodicity cells, $a = Q(\alpha)$ is only defined up to a sign. There are two ways to bypass this issue. The first and obvious one (see [11]) would be to determine a coherent orientation of $a$ over $D$ (what could be done proceeding from one triangle to its neighbors and so on). The second option is based on the introduction of a covering space $\mathcal{D}$ over $D$ and to define $\varphi$ on $\mathcal{D}$ rather than on $D$ itself (we will give more details soon). A minor advantage of this second approach relies on the fact that it saves us the computation of a coherent rotation field $a$. More important, even if we discard this possibility in the current article, such a coherent orientation does not necessarily exists in the presence of singularities like the ones displayed in Figure 14). Hence, the first option can not be extended to encompass the general case contrarily to the second one that we retain here (a rapid description of the way the singularities could be treated in this context can be found in [19]). In this section, we introduce the manifold $\mathcal{D}$ and recast the problem that defines the grid map. The reader mainly interested in the practical implementation could skip this part for section 5.5.

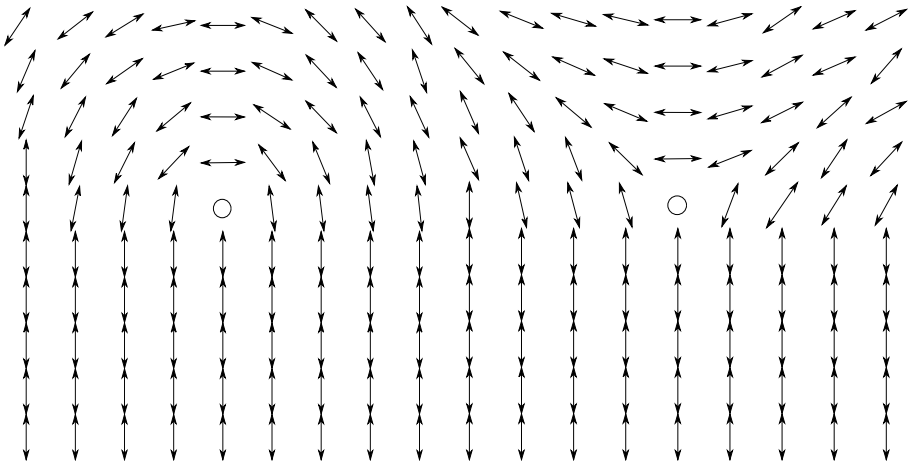

(a) Positive singularity (b) Negative singularity

Figure 14: The two canonical type of singularities of the field $a_1$. The field $a_1$ is not coherently orientable in those cases, as the vector $a_1$ rotates of an angle of $\pm\pi$ along circles which are enclosing the singularities.

**An abstract manifold.** We introduce the cover space of $D$

$$\mathcal{D} = \{(x, T) \in D \times \mathrm{SO}(2) \text{ such that } T^2 = b(x)\},$$

where $\mathrm{SO}(2)$ is the set of rotations in $\mathbb{R}^2$. It is a submanifold of the space $D \times \mathrm{SO}(2)$. The rotation field $a$ is assume to be locally orientable, meaning that $D$ can be covered by open sets $U$ for each of which there exists a map $T_U \in \mathcal{C}(U, \mathrm{SO}(2))$ such that for all $x \in U$, $T_U(x)^2 = b(x)$. The map $T_U$ defines two charts $g_U^+$ and $g_u^-$ of the manifold $\mathcal{D}$ given by

$$\begin{array}{rcl} g_U^+ : U & \to & \mathcal{D} \\ x & \mapsto & (x, T_U(x)) \end{array} \quad \text{and} \quad \begin{array}{rcl} g_U^- : U & \to & \mathcal{D} \\ x & \mapsto & (x, -T_U(x)). \end{array} \tag{25}$$

In the present article, we assume the rotation field $a$ of the optimal design to be without singularities (and thus orientable). Thus, $\mathcal{D}$ is simply the union of two copies of $D$ consisting of the two possible orientations of $a$. Nevertheless, we will not use this feature in the following. Its makes our method relatively easy to extend so to encompass the case with singularities, what will be done in a future work. Before digging into deeper details in the next section, let us illustrate how $\mathcal{D}$ can be represented if the field $a$ contains singularities.

The Figure 15 gives such a representation of the manifold $\mathcal{D}$ in the presence of a negative singularity. The manifold $\mathcal{D}$ is obtained starting with two copies of the initial domain $D$ (a square in the present case). Each of them is cut along the same path connecting the singularity to the boundary of $D$. Then, they are glued together along this very path. On Figure 15 the thick (respectively

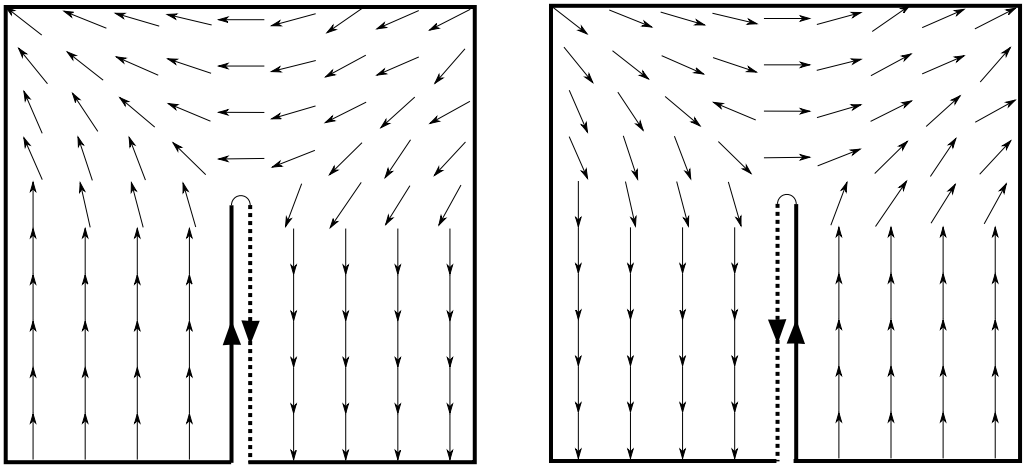

Figure 15: Representation of the manifold $\mathcal{D}$ in the presence of a singularity.

the dotted) lines are glued together. Contrarily to the case without singularity, $\mathcal{D}$ is connected but not simply connected and can not be embedded in $\mathbb{R}^2$. Another representation of $\mathcal{D}$ is given by the Figure 16 as a submanifold of $D \times \mathrm{SO}(2) \simeq D \times \mathbb{R}/2\pi\mathbb{Z}$. In this case, the manifold $\mathcal{D}$ looks as a screw in the cylinder $D \times (0, 2\pi)$ whose axis is parallel to the $z$-direction and located at the very position of the singularity in $D$. The top and bottom parts of the screw are identified.

Finally, we endow $\mathcal{D}$ with a differential structure through the projection $p_D$ onto $D$. In particular, it induces a gradient operator on $\mathcal{D}$ and a second linear form $p_D^*(\,\mathrm{dx})$, the pull-back of second linear form $\,\mathrm{dx}$ defined on $D$. For sake of simplicity, we will denote $p_D^*(\,\mathrm{dx})$ simply $\,\mathrm{dx}$ in the following.

**Construction of $\varphi$.** We change our working space from $D$ to $\mathcal{D}$, meaning that we are now seeking for a grid map $\varphi$ from $\mathcal{D}$ into $\mathbb{R}^2$ such that

$$\nabla\varphi = e^r T \tag{26}$$

for all $(x, T) \in \mathcal{D}$ and for some function $r(x)$. The operator $\nabla$ in (26) is not the standard gradient on the manifold $\mathcal{D}$ but is rather defined by

$$\nabla\varphi(x, T) = \nabla\varphi_U(x),$$

where $U$ is an open subset of $D$,

$$\varphi_U(x) = \varphi \circ g_U(x),$$

and $g_U$ is a chart of the neighborhood of $(x, T)$ like in (25). Moreover, without loss of generality, we can assume that

$$\varphi(x, -T) = -\varphi(x, T). \tag{27}$$

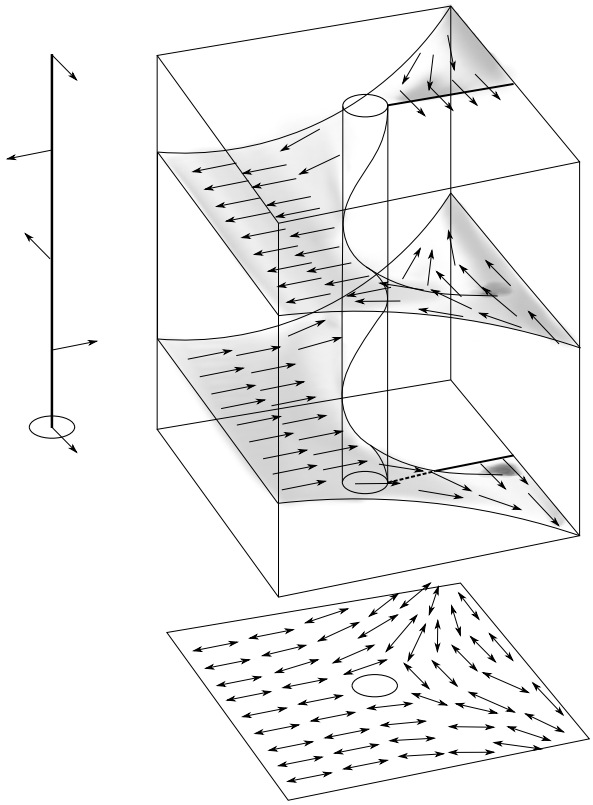

Figure 16: Submanifold $\mathcal{D}$ in $D \times \mathbb{R}/2\pi\mathbb{Z}$.

Indeed, if $\varphi$ satisfies (26), then the map $(x,T) \mapsto (\varphi(x,T) - \varphi(x,-T))/2$ still satisfies (26) together with the antisymmetric property (27). Thus, if the conformality condition (16) is satisfied, the map $\varphi$ can be defined as the solution of

$$\min_{\varphi \in \mathcal{V}} \int_{\mathcal{D}} |\nabla \varphi - e^r T|^2 \, \mathrm{dx}, \tag{28}$$

over the maps $\varphi$ in

$$\mathcal{V} := \left\{ \varphi \in H^1(\mathcal{D}; \mathbb{R}^2) \text{ such that } \varphi(x,-T) = -\varphi(x,T) \text{ for all } (x,T) \in \mathcal{D} \right\}.$$

Previously in this section we assumed that $D$ can be covered by open sets $U$ where the rotation field $a$ is coherently orientable. From now on, let us be more specific in assuming that those open sets $U$ are the cells $K$ of a mesh covering $D$. In other words, there exists a finite family $\mathcal{T}$ of disjoint open subsets $K$ such that

$$\overline{D} = \cup_{K \in \mathcal{T}} \overline{K},$$

and such that the rotation field $a$ is coherently orientable on all $K$. We denote $T_K : K \to \mathrm{SO}(2)$ such an orientation on $K$. We have

$$\begin{aligned} \int_{\mathcal{D}} |\nabla \varphi - e^r T|^2 \, \mathrm{dx} &= \sum_{K \in \mathcal{T}} \int_{p_D^{-1}(K)} |\nabla \varphi - e^r T|^2 \, \mathrm{dx} = \\ &\sum_{K \in \mathcal{T}} \int_{g_K^+(K) \cup g_K^-(K)} |\nabla \varphi - e^r T|^2 \, \mathrm{dx} \\ &= \sum_{K \in \mathcal{T}} \int_K \left| \nabla(\varphi \circ g_K^+) - e^r T_K(x) \right|^2 \mathrm{dx} + \int_K \left| \nabla(\varphi \circ g_K^-) + e^r T_K(x) \right|^2 \mathrm{dx} \end{aligned}$$

with $g_K^{\pm} = \mathrm{Id} \times (\pm T_K)$. In particular, for all $\varphi \in \mathcal{V}$, due to the antisymmetry condition, we get

$$\int_{\mathcal{D}} |\nabla \varphi - e^r T|^2 \, \mathrm{dx} = 2 \sum_{K \in \mathcal{T}} \int_K \left| \nabla(\varphi \circ g_K^+) - e^r T_K(x) \right|^2 \mathrm{dx}. \tag{29}$$

## 5.5 Practical computation of the grid map $\varphi$

Solving (28) using a classical finite element software seems at first sight far form straightforward, mainly because the solution $\varphi$ is defined over the manifold $\mathcal{D}$ and not a two dimensional open subset of $\mathbb{R}^2$.

We use $P_1$ finite elements to discretize $\varphi$. To build the bilinear form of the variational formulation, we introduce an interpolation operator from $\mathcal{V}_h$, the Lagrange finite elements of degree one on $\mathcal{D}$ that satisfies the antisymmetry condition (27), onto the space $W_h$ of $P_1$ discontinuous Galerkin elements on $D$.

**The finite element space $\mathcal{V}_h$.** Let $\mathcal{T}_h$ be a regular mesh of $D$. We assume that on each triangle $K$ of the mesh, the rotation field $a$ is locally orientable, meaning that, on each $K$, there exists a regular map $T_K$ with values in SO(2) such that

$$T_K(x)^2 = b(x) \text{ for all } x \in K. \tag{30}$$

Such a coherent orientation field $T_K$ is easy to define and more details are given at the end of this section. We also choose an orientation $T_i$ at each vertex $x_i$ of the mesh such that

$$T_i^2 = b(x_i). \tag{31}$$

The manifold $\mathcal{D}$ can be endowed with a mesh, whose elements are $g_K^+(K) = (\mathrm{Id} \times T_K)(K)$ and $g_K^-(K) = (\mathrm{Id} \times (-T_K))(K)$ and whose vertices are $(x_i, T_i)$ and $(x_i, -T_i)$, where $x_i$ spans the vertices of $\mathcal{T}_h$ and $K$ its triangles. A $P_1$ finite element on $\mathcal{D}$ is defined by its values on the nodes $(x_i, T_i)$ and $(x_i, -T_i)$. Moreover, for any element $\varphi \in \mathcal{V}_h$ we have from (27)

$$\varphi(x_i, -T_i) = -\varphi(x_i, T_i).$$

Thus $\varphi \in \mathcal{V}_h$ is uniquely determined by the values $\varphi(x_i, T_i)$. It follows that $\mathcal{V}_h$ is of the same dimension than $V_h$, the space of $P_1$ Lagrange finite elements over $D$. An element $\varphi \in \mathcal{V}_h$ is completely defined by a vector $\{\varphi\}$ of coordinates

$$\varphi_i = \varphi(x_i, T_i).$$

**The finite element space $W_h$.** We denote by $W_h$ the space of $P_1$ discontinuous finite elements on $D$ with values in $\mathbb{R}^2$. Any element $\psi \in W_h$ is uniquely defined by its values at each vertices of each triangle $K \in \mathcal{T}_h$, that is by a vector

$$\psi_{3k+l} = \psi|_{K_k}(x_i),$$

with $k$ the index of the $k$-th triangle $K_k$ of $\mathcal{T}_h$ and $x_i$ is the $l$-th vertex of the triangle $K_k$ (where $l \in \{0, 1, 2\}$).

**The interpolation $I^h$ from $\mathcal{V}_h$ onto $W_h$.** We are now in a position to introduce an interpolation operator $I^h$ from $\mathcal{V}_h$ (the $P_1$ antisymmetric finite elements on $\mathcal{D}$ with values in $\mathbb{R}^2$) onto $W_h$ (the $P_1$ Galerkin discontinuous finite elements over $D$ with values in $\mathbb{R}^2$). Let $\varphi$ be an element of $\mathcal{V}_h$. For all triangle $K \in \mathcal{T}_h$, we define

$$(I^h\varphi)|_K = \varphi \circ g_K^+. \tag{32}$$

We recall that $g_K^+ = \mathrm{Id} \times T_K$ as in (25). In other words, the restriction of $I^h\varphi$ to $K$ is equal to the restriction of $\varphi$ on the corresponding triangle endowed with the chosen orientation $T_K$.
From a practical point of view, the interpolation matrix from $\mathcal{V}_h$ to $W_h$ is sparse and defined for all index $k$ of a triangle, for all $l \in \{0, 1, 2\}$ and for all index $i$ of a vertex by

$$I^h_{3k+l,i} = \begin{cases} +1 & \text{if } T_i = \ \ T_{K_k}(x_i) \text{ and } x_i \text{ is the } l\text{-th vertex of } K_k \\ -1 & \text{if } T_i = -T_{K_k}(x_i) \text{ and } x_i \text{ is the } l\text{-th vertex of } K_k \\ 0 & \text{if } x_i \text{ is not the } l\text{-th vertex of } K_k \end{cases} \tag{33}$$

**Computation of $\varphi$.** The map $\varphi$ from $\mathcal{V}_h$ into $\mathbb{R}^2$ is the minimizer of

$$G(\varphi) := \int_{\mathcal{D}} |\nabla\varphi - e^r T|^2 \, \mathrm{dx}\,.$$

We recall that from (29) that

$$G(\varphi) = 2 \sum_{K\in\mathcal{T}_h} \int_K \left|\nabla(\varphi \circ g_K^+) - e^r T_K(x)\right|^2 \, \mathrm{dx}\,.$$

Thanks to (32), this functional can be rewritten as

$$G(\varphi) = 2 \sum_{K\in\mathcal{T}_h} \int_K |\nabla I^h(\varphi) - e^r T_K|^2 \, \mathrm{dx}\,.$$

Thus, the minimizer is the solution of the variational formulation consisting in finding $\varphi \in \mathcal{V}_h$ such that for all for all $\psi \in \mathcal{V}_h$,

$$\sum_{K\in\mathcal{T}_h} \int_K \nabla I^h(\varphi) : \nabla I^h(\psi) \, \mathrm{dx} = \sum_{K\in\mathcal{T}_h} \int_K e^r T_K : \nabla I^h(\psi) \, \mathrm{dx}\,.$$

Introducing the bilinear form

$$\mathcal{A}(\Phi, \Psi) = \sum_{K\in\mathcal{T}_h} \int_K \nabla\Phi : \nabla\Psi \ \mathrm{dx} \tag{34}$$

on $W_h$ and the linear form (also on $W_h$)

$$L(\Psi) = \sum_{K\in\mathcal{T}_h} \int_K e^r T_K : \nabla\Psi \, \mathrm{dx}, \tag{35}$$

The map $\varphi \in \mathcal{V}_h$ is such that for all $\psi \in \mathcal{V}_h$,

$$\mathcal{A}(I^h(\varphi), I^h(\psi)) = L(I^h(\psi)). \tag{36}$$

It only requires to assemble the matrices associated with the bilinear and linear forms $\mathcal{A}$ and $L$ on the space of Galerkin discontinuous functions to obtain the system satisfied by $\varphi$.

**Remark 5.** *If (as we consider here), the rotation field of the periodicity cells is coherently orientable, the manifold $\mathcal{D}$ is made of two disconnected copies of $D$ and $\varphi$ is defined up to a constant. This constant can be fixed by adding a small penalization of the $L^2$-norm of $\varphi$ in the definition of the bilinear form $\mathcal{A}(\cdot,\cdot)$,*

$$\mathcal{A}(\Phi, \Psi) = \sum_{K\in\mathcal{T}_h} \int_K \left(\nabla\Phi : \nabla\Psi + \eta^2 \Phi \cdot \Psi\right) \mathrm{dx},$$

*with $0 < \eta \ll 1$.*

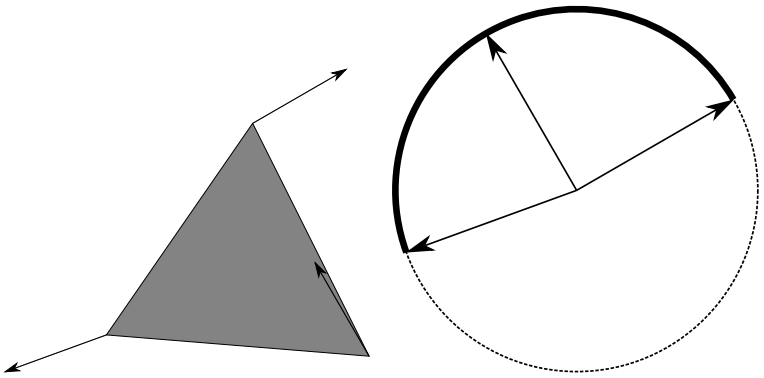

(a) Field $b$ on a triangle ... (b) ... and its image in $S^1$.

Figure 17: Field $b_1 = (\cos(\beta), \sin(\beta))$ that defines the rotation of the periodicity cells.

**Coherent local orientation.** It remains to determine a local coherent orientation on each triangle of the mesh in order to be able to define the interpolation operator $I^h$ form $\mathcal{V}_h$ onto $W_h$.

Let us consider a practical example. We recall that the output of the homogenization step is a rotation field $b$. During this phase of the optimization, we use $P_1$ Lagrange finite elements to discretized this field. Hence, we can consider each triangle of the mesh separately.

Figure 17(a) displays the vector field $b_1$ on the nodes of a triangle, while Figure 17(b) shows the image of this field on $S^1$ (the bold part of the circle). We have now to choose coherent values of the vector $a_1$ on each node of this triangle (we recall that $a^2 = b$). Two choices are possible at each node of the triangle as illustrated by Figure 18. This leads to eight options for the orientation of the triangle. If the triangle does not contain any singularity, two of them define a coherent orientation (see Figure 19). The possible orientations of $a_1$ are simply obtained by the condition that the scalar product between all couples of values taken by the vector $a_1$ at nodes should be positive. Hence, it suffices to choose an arbitrary orientation for one vertex and to orient the others accordingly. Doing so, we obtain a rotation field $T_K$ on each triangle $K$. Note that the chosen orientation is not continuous from on triangle to the other. Moreover, such a coherent orientation does not exists if the triangle contains a singularity, a case that is disregarded in this article.

**Sequence of shapes.** In conclusion, after the regularization algorithm described in section 5.3, the sequence of shapes is constructed in three steps

1. Choosing a coherent orientation $T_K$ on each triangle and an orientation $T_i$ on each vertex of the mesh $\mathcal{T}_h$ of the working domain $D$ (30-31).

2. Build the interpolation matrix $I^h$ defined by (33).

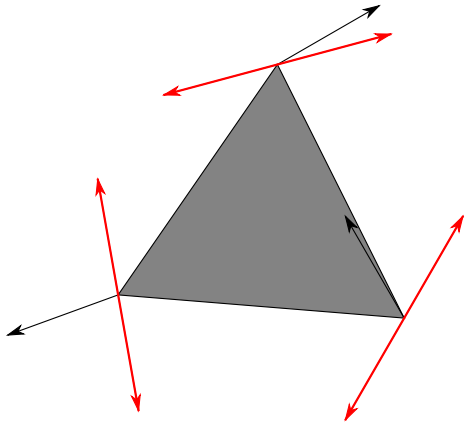

Figure 18: Field $a_1 = (\cos(\alpha), \sin(\alpha))$ is defined up to a sign at the nodes.

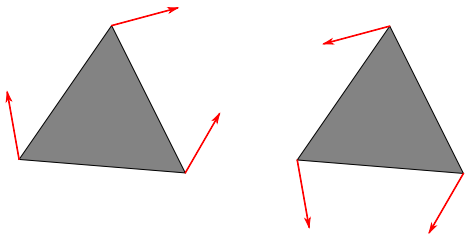

Figure 19: The two possible orientations of $a_1$ on a triangle.

3. Build the matrix $A^h$ and the vector $L^h$ in the space of $P_1$ discontinuous finite elements associated to the bilinear and linear forms $\mathcal{A}$ and $L$ (34-35).

4. Compute the component $\{\varphi\} = (\varphi_i)$ of the coordinates of grid map $\varphi$ in the base of $\mathcal{V}_h$ defined by the chosen orientation $T_i$.

$$(I^h)^T A^h I^h \{\varphi\} = L^h I^h$$

5. The sequence of shapes is implicitly defined by (12-14)

$$\Omega_\varepsilon(\varphi, m) = \Omega_\varepsilon(I_h(\varphi), m) = \{x \in D \text{ such that } F_\varepsilon^{I_h(\varphi),m} \leq 0\}.$$

**Remark 6.** *Both $\Omega_\varepsilon(\varphi, m)$ and $\Omega_\varepsilon(I_h(\varphi), m)$ do define the same sequence of shapes due to the antisymmetry property of the grid map $\varphi$.*

**Remark 7.** *In all our examples the computational domain $D$ is a simply connected domain in the plane (i.e., without holes). The connectivity property of $D$ does not play any role in the pre-processing and processing steps (see Sections 3 and 4) but it has some impact in the present post-processing step. In particular, Lemma 5.1 (about the conformality condition on the angle $\alpha$) is stated only for simply connected domains. This is linked somehow to the singularity issue: for example, a radial vector field has a singularity at the origin in a ball but no singularity in a corona. Therefore, the conformality condition, as well as the presence and the removal of singularities, are different for domains with or without holes. The generalization of our algorithm in such a case is work under progress. Note that it is not difficult to take into account non-optimizable zones where the material density is fixed, either to 1 or to 0 (more precisely, to the minimal value imposed by the upper bound $1 - 10^{-3}$ imposed on the microstructure parameters $m_i$). In such a case, the conformality condition is enforced everywhere in the domain $D$, including the non-optimizable zones.*

## 5.6 Numerical results

We implemented the above algorithm in Freefem++ [13]. Here, we consider the bridge test case. The computed map $\varphi$ is displayed in Figure 20. However, $\varphi$ is defined up to its sign on $D$. Hence for better readability of the figures, we displayed the absolute value of $\varphi$. On Figure 20(a) (resp. 20(b)), the vector $a_2$ (resp. $a_1$) is also displayed. Hence, we can easily check that the isolines of $|\varphi_i|$ are orthogonal to the vector $a_i$. The computed map $\varphi$ respects the regularized optimal orientation of the microstructure. On Figure 21 one can check that the regular square grid, projected by $\varphi$, is conformal, namely all lines cross at right angles.

The sequence of genuine or classical shapes can now be constructed using the simple formulas (12), (14). We displayed in Figure 22 several shapes $\Omega_\varepsilon(\varphi, m)$ for various values of $\varepsilon$. Those shapes are very smooth. They feature rectangular holes, oriented according to $\alpha$. The smaller $\varepsilon$, the closer from the homogenized optimal design the shape $\Omega_\varepsilon(\varphi, m)$ is.

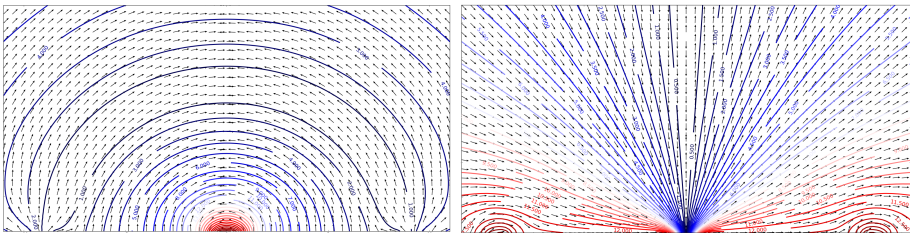

(a) $|\varphi_1|$ and $a_2$ (b) $|\varphi_2|$ and $a_1$

Figure 20: Map $\varphi$ (isolines) and the vectors $a_i$ (arrows) for the bridge case

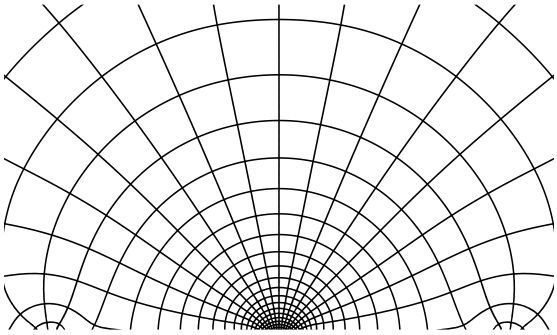

Figure 21: Projection of a regular grid through the map $\varphi$ for the bridge case

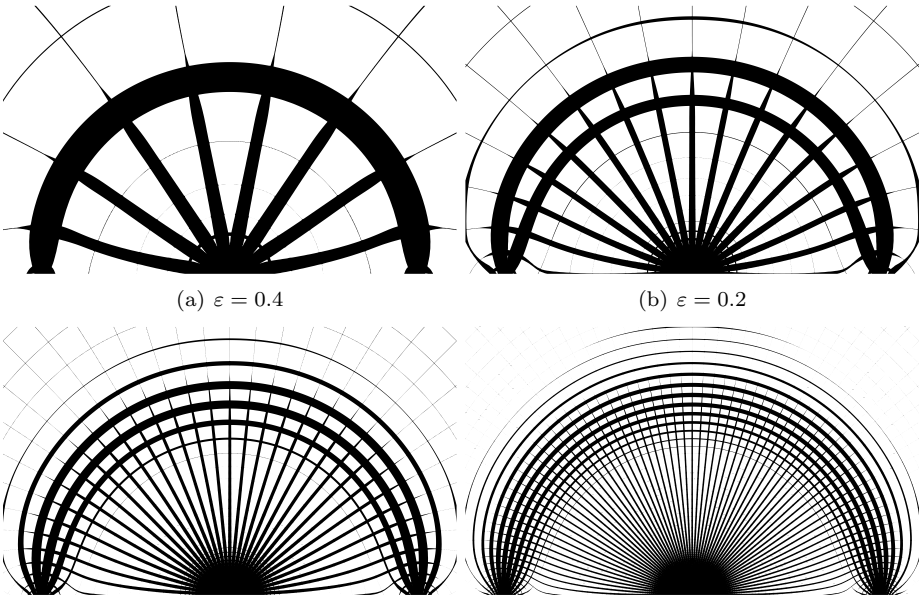

(a) $\varepsilon = 0.4$ (b) $\varepsilon = 0.2$

(c) $\varepsilon = 0.1$ (d) $\varepsilon = 0.05$

Figure 22: $\Omega_\varepsilon(\varphi, m)$ for several $\varepsilon$ in the case of the bridge

For the sake of comparison, the elasticity problem for each of these classical shapes has been solved on a fine mesh (316 250 elements), using the same ersatz material for void than in the optimization process (0.1% of the elastic tensor of the isotropic material). The resulting compliances for various values of the cell characteristic size $\varepsilon$ are displayed on Figure 23 (each dot corresponds to one value of $\varepsilon$). Their relative volume, defined as the ratio between the actual volume of the shape and the target one, is also plotted. The compliance of the genuine shapes is close to the optimal value of the homogenized design but slightly above. As soon as $\varepsilon$ is small enough, these compliances are lower than that for an optimized shape using no lattice material (here, the reference is the shape obtained by the SIMP method, see Figure 9). The variations of the compliance are mostly caused by the variations of the volume. Indeed, a smaller volume induces a larger compliance. As a matter of fact, the projection post-processing phase does not ensure a preservation of the total volume. However, such volume errors are smaller for smaller $\varepsilon$. Nevertheless, for too small values of $\varepsilon$, the mesh may not be fine enough to capture acurately the details of the shapes, which can alter the evaluation of the compliance. Note that the compliance values for the SIMP design and the homogenized design are computed on a coarser mesh. But we check that their compliances on the fine mesh are almost the same (the relative differences are of the order of 1%).

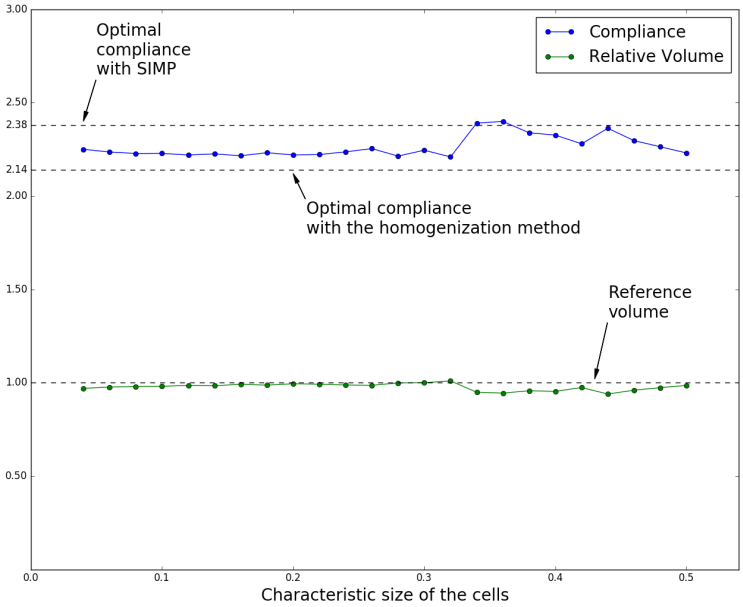


Figure 23: Compliance and relative volume of the genuine shapes according to the cell characteristic size $\varepsilon$

## 5.7 Post-processing of the final structures

The above shapes are not straightforwardly manufacturable. Indeed, they can feature very thin bars, some of them not even connected to the principal structure, as well as very tiny holes. We propose here a simple post-treatment in order to get manufacturable shapes. More clever ideas could certainly be implemented but we leave this to future work.

Let $h_{min} > 0$ be the minimal manufacturable lengthscale or feature size, meaning the smallest possible width of bars and diameter of holes which can be effectively built. We do not allow for details or features smaller than $h_{min}$ in the post-processed shape. Recall that $\varepsilon$ is our choice of a global size of cells. Then, locally after deformation, the cell size is $h_c(x) = \varepsilon e^{-r(x)}$, which is varying from point to point. Hence, the local widths of bars and holes are respectively given by $(1 - m_i(x))h_c(x)$ and $m_i(x)h_c(x)$.

In the following, we distinguish two regimes, depending of the local size of the cell $h_c(x)$. First, if the local cell size is too small, a hole and a bar of minimal width cannot coexist: we have to choose between a completely full or void cell. Hence, if $h_c < 2h_{min}$, a thresholding is applied separately to each field $m_i$: it is assigned the value 0 if $m_i < 0.5$ and 1 otherwise.

Second, when $h_c \geq 2h_{min}$, our post-processing criteria about the widths of

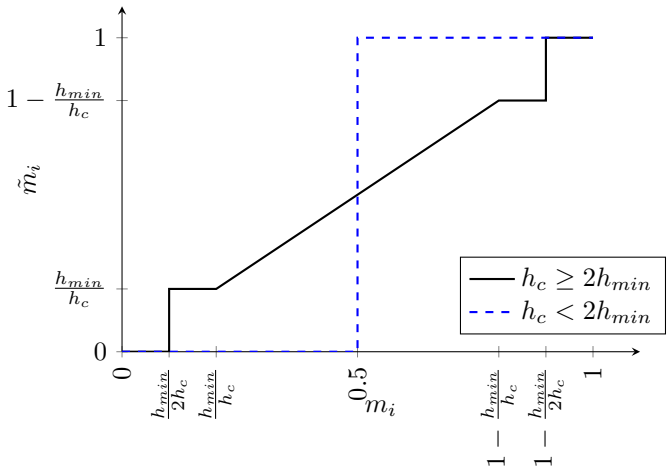


Figure 24: Thresholds for the post-treatment, or $\tilde{m}_i$ as a function of $m_i$, in order to fulfill a minimal feature size $h_{min}$

the bar and the hole is satisfied if:

$$\forall i \in \{1,2\} \quad \frac{h_{min}}{h_c} \leq m_i \leq 1 - \frac{h_{min}}{h_c}\,. \tag{37}$$

Failing (37), we simply threshold the values of $m_1$ and $m_2$, according to the functions displayed on Figure 24 in order to reach void or full material.
The thresholded $m$ is then denoted $\tilde{m}$.

Let $O_\varepsilon(\varphi,\tilde{m})$ be the shape obtained from $\Omega_\varepsilon(\varphi,\tilde{m})$ by filling its closed holes, see Figure 25(e). Numerically, the complement of $O_\varepsilon(\varphi,\tilde{m})$ is computed step by step, by evaluating the sign of $F_\varepsilon^{\varphi,\tilde{m}}$. If it is positive, the current vertex belongs to the complement $O_\varepsilon^c(\varphi,\tilde{m})$ and then its neighbors, which are not already visited, are added to a list of vertices, which should be tested. Otherwise, the current vertex does not belong to $O_\varepsilon^c(\varphi,\tilde{m})$: no particular action is required and so we keep going with the next vertex of our list.

Then, the subset $O_\varepsilon(\varphi,\tilde{m})$ is regularized in order to remove the disconnected bars or the bars that have one free end point. Numerically, we explore all the vertices of the complement as follows. For any given vertex, we check all other vertices not further away than a distance $h_{min}$: if this vertex belongs to the complement too, all vertices between them are added to the complement. In this way, we suppress all disconnected bars and all bars that have one free end point, which are not too wide, of $O_\varepsilon(\varphi,\tilde{m})$. This new subset is denoted $\tilde{O}_\varepsilon(\varphi,\tilde{m})$, see Figure 25(f).

Finally, the post-processed structure is given by the intersection $\tilde{\Omega}_\varepsilon(\varphi,\tilde{m}) = \Omega_\varepsilon(\varphi,\tilde{m}) \cap \tilde{O}_\varepsilon(\varphi,\tilde{m})$, see Figure 25(g). Several post-processed structures $\tilde{\Omega}_\varepsilon(\varphi,\tilde{m})$ for the bridge case are displayed on Figure 26.

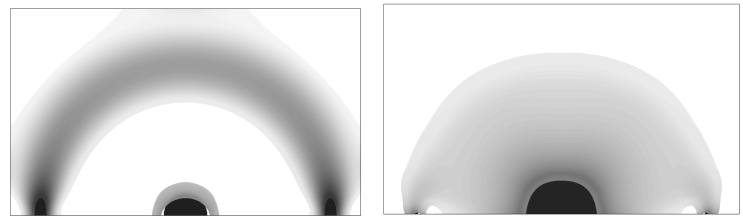

(a) $\tilde{m}_1$



(b) $\tilde{m}_2$

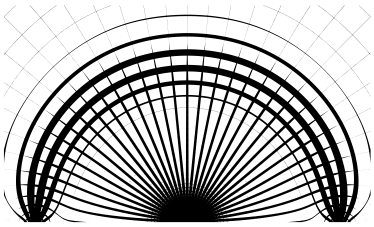

(c) $\Omega_\varepsilon(\varphi, m)$, without threshold

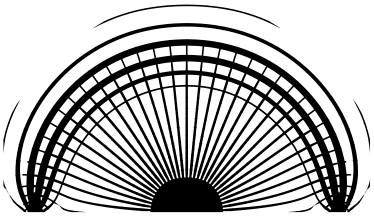

(d) $\Omega_\varepsilon(\varphi, \tilde{m})$, with threshold

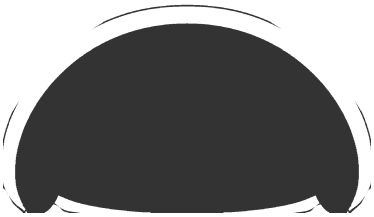

(e) $O_\varepsilon(\varphi, \tilde{m})$

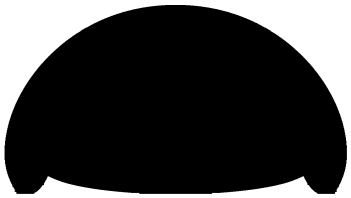

(f) $\tilde{O}_\varepsilon(\varphi, \tilde{m})$

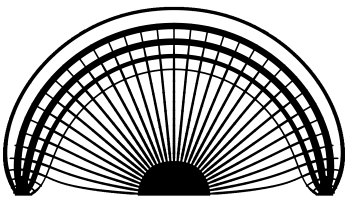

(g) Post-processed structure $\Omega_\varepsilon(\varphi, \tilde{m})$

Figure 25: Results of the post-treatment for the bridge case, with a minimal feature size $h_{min} = 0.05\varepsilon$ (here : $\varepsilon = 0.1$)

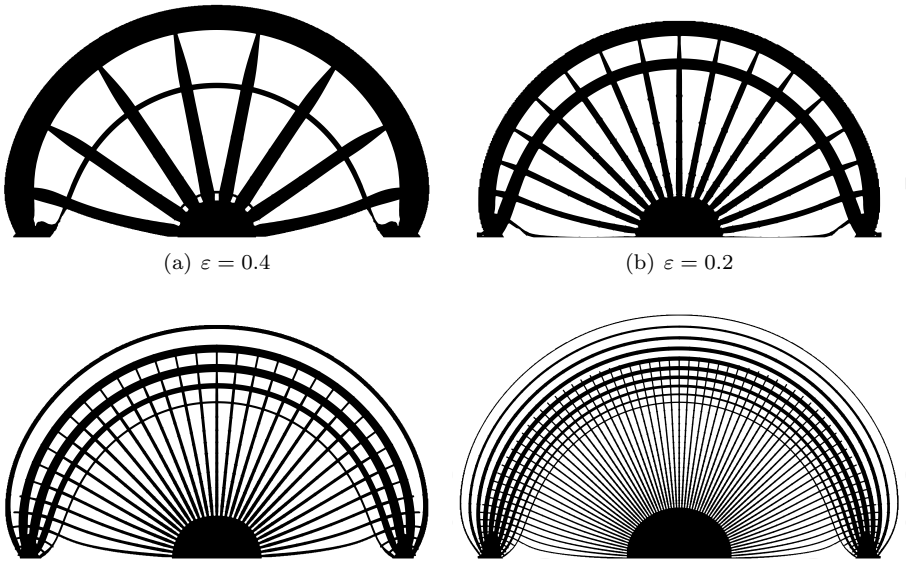

(a) $\varepsilon = 0.4$ (b) $\varepsilon = 0.2$

(c) $\varepsilon = 0.1$ (d) $\varepsilon = 0.05$

Figure 26: Post-processed structures $\tilde{\Omega}_\varepsilon(\varphi, \tilde{m})$ for several $\varepsilon$ in the case of the bridge

# 6 Other numerical examples

We applied the whole method to the several cases: optimization of an arch (Figure 27), a cantilever (Figure 28), a MBB beam (Figure 29) and a L-beam (Figure 30). As in the case of the bridge, used previously to illustrate our approach, the volume constraint is fixed to 30% of the working domain and the number of iterations during the optimization – before regularization – is set to 200. The number of vertices is in all cases, lower than 9000 and the numbers of triangles to 18000.

For the arch (Figure 27) the domain size is $22 \times 13$ and a unit vertical load is applied at the middle of the bottom border on an interval of length 2. The Dirichlet boundary condition is applied on two symmetric intervals of length 1 starting at a distance 1 from the sides. The resulting compliance for the homogenized design is 1.558.

For the cantilever (Figure 28), the domain size is $20 \times 20$. The Dirichlet boundary condition is applied on a central interval of length 10 on the left side. A unit vertical load is applied in the center of its right side on a segment of length 1. The resulting compliance for the homogenized design is 2.729.

For the MBB beam (Figure 29), the domain size is $30 \times 10$. We took advantage of the symmetry, by running the algorithm just on the half of a complete beam. Then the structure is allowed to slide on its left side. A unit vertical load is applied in the upper left corner on a segment of length 1. The resulting compliance for the homogenized design is 13.626

For the L-beam (Figure 30), the domain size is $10 \times 10$. The structure is clamped on its upper side, and is submitted to a unit vertical load in the center of its right side on a segment of 20% of the total length. The resulting compliance for the homogenized design is 6.581.

For each case, we have represented: (a) the applied loads and the boundary conditions; (b-c) the optimal orientation of the periodicity cells before and after regularization; (d) the underlying lattice on which the optimal composite is built; (e-g) the optimal density and microstructure parameters; (h-j) the sequence of shapes before post-processing, and after (k-n).

The orientation fields of all those cases do not feature any singularity after regularization, which is a necessary condition for our method to apply. In the case of the L-beam, the orientation field in Figure 30(b) presents two singularities. Both have been ejected during the regularization step as seen on Figure 30(c). Note that the orientation field before and after regularization are significantly different (it turns with an angle of order $\pi/2$ on some areas). We would like to draw the attention of the reader to the fact that it is not universal: in some cases, no matter how strong the regularization is chosen, singularities do persist. We perform a last test case, the so-called electrical mast (see Figure 31), to illustrate this fact: two negative singularities, located inside the domain, cannot neither be removed nor pushed toward the boundary during the regularization step (see Figure 31(b)). The application of our method failed in this case, as it is not designed to deal with the presence of singularities. This is illustrated by Figure 31(c), where the computed grid is clearly not correctly aligned

with the optimal orientation of the cells in the vicinity of the singularities. To overcome this problem, at least two different strategies can be considered. One consists in modifying the regularization in a way that force more effectively the singularities to be eliminated. For instance, this can be done by adding a penalization of the singularities to the cost function. We have implemented such a method and are indeed able to remove the singularities from the optimal shape as shown in Figures 31(d) and 31(e). Another option, already mentioned previously, is to adapt the projection step so that it is able to take singularities into account. These approaches are not presented here, but will be the topic of a future article [10].

## Acknowledgments

P. G. D. is a CIFRE PhD student, funded by SAFRAN, the support of which is kindly acknowledged. G. A. is a member of the DEFI project at INRIA Saclay Ile-de-France. The work of G. A. is partially supported by the SOFIA project, funded by BPI (Banque Publique d'Investissement).

## References

[1] G. Allaire. *Shape optimization by the homogenization method*, volume 146 of *Applied Mathematical Sciences*. Springer-Verlag, New York, 2002.

[2] G. Allaire, E. Bonnetier, G. Francfort, and F. Jouve. Shape optimization by the homogenization method. *Numer. Math.*, 76(1):27–68, 1997.

[3] G. Allaire, F. Jouve, and A.-M. Toader. A level-set method for shape optimization. *C. R. Math. Acad. Sci. Paris*, 334(12):1125–1130, 2002.

[4] G. Allaire and O. Pantz. Structural optimization with FreeFem++. *Struct. Multidiscip. Optim.*, 32(3):173–181, 2006.

[5] C. Barbarosie and A.-M. Toader. Shape and topology optimization for periodic problems. II. Optimization algorithm and numerical examples. *Struct. Multidiscip. Optim.*, 40(1-6):393–408, 2010.

[6] M. P. Bendsøe. Optimal shape design as a material distribution problem. *Structural and multidisciplinary optimization*, 1(4):193–202, 1989.

[7] M. P. Bendsøe and N. Kikuchi. Generating optimal topologies in structural design using a homogenization method. *Comput. Methods Appl. Mech. Engrg.*, 71(2):197–224, 1988.

[8] M. P. Bendsøe and O. Sigmund. *Topology optimization*. Springer-Verlag, Berlin, 2003. Theory, methods and applications.

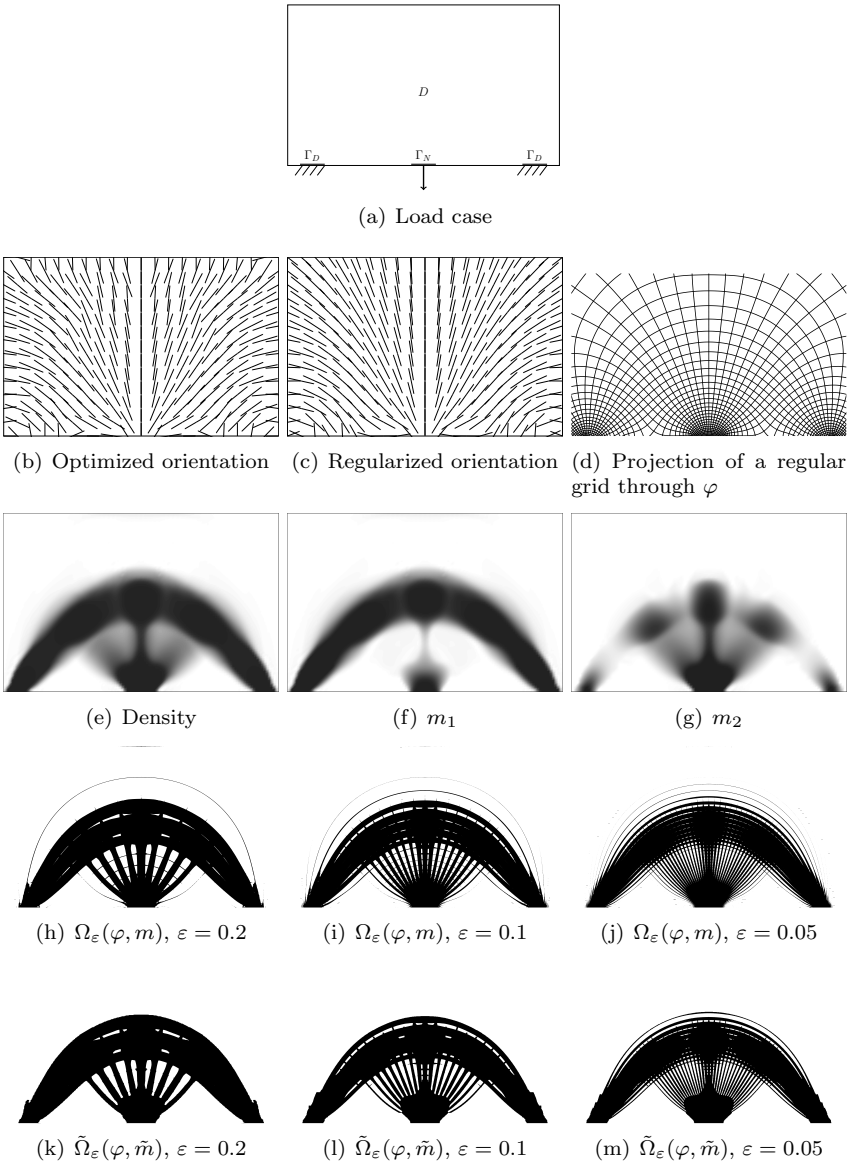


(a) Load case

(b) Optimized orientation (c) Regularized orientation (d) Projection of a regular grid through $\varphi$

(e) Density (f) $m_1$ (g) $m_2$

(h) $\Omega_\varepsilon(\varphi, m)$, $\varepsilon = 0.2$ (i) $\Omega_\varepsilon(\varphi, m)$, $\varepsilon = 0.1$ (j) $\Omega_\varepsilon(\varphi, m)$, $\varepsilon = 0.05$

(k) $\tilde{\Omega}_\varepsilon(\varphi, \tilde{m})$, $\varepsilon = 0.2$ (l) $\tilde{\Omega}_\varepsilon(\varphi, \tilde{m})$, $\varepsilon = 0.1$ (m) $\tilde{\Omega}_\varepsilon(\varphi, \tilde{m})$, $\varepsilon = 0.05$

Figure 27: Complete process for an arch case

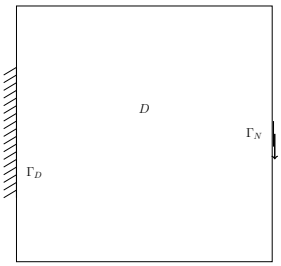


(a) Load case

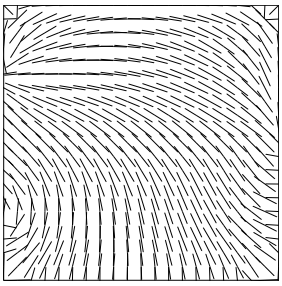

(b) Optimized orientation

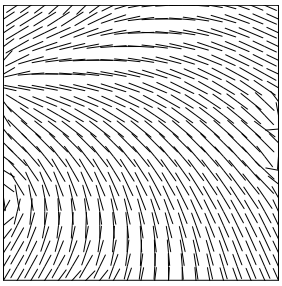

(c) Regularized orientation

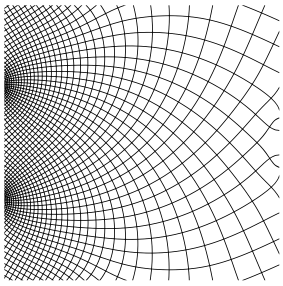

(d) Projection of a regular grid through $\varphi$

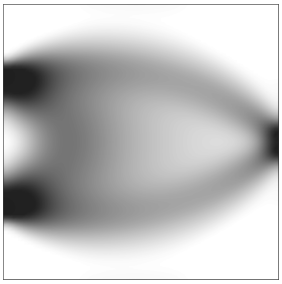

(e) Density

(f) $m_1$

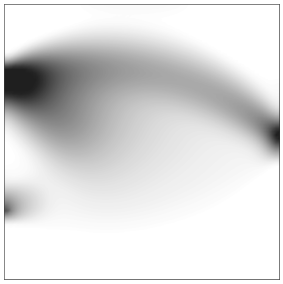

(g) $m_2$

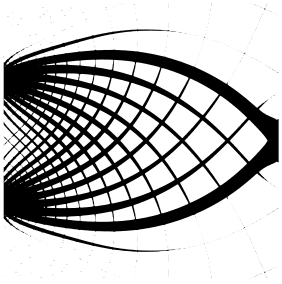

(h) $\Omega_\varepsilon(\varphi, m)$, $\varepsilon = 0.2$

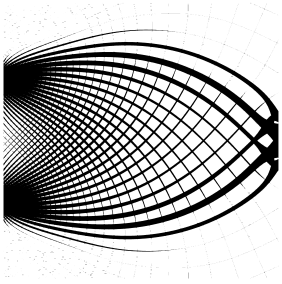

(i) $\Omega_\varepsilon(\varphi, m)$, $\varepsilon = 0.1$

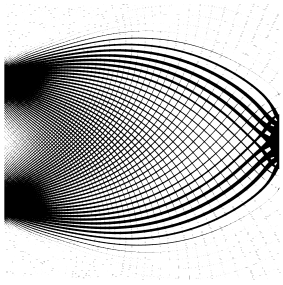

(j) $\Omega_\varepsilon(\varphi, m)$, $\varepsilon = 0.05$

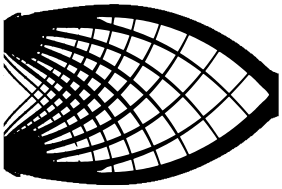

(k) $\tilde{\Omega}_\varepsilon(\varphi, \tilde{m})$, $\varepsilon = 0.2$

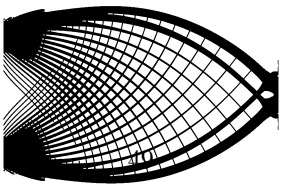

(l) $\tilde{\Omega}_\varepsilon(\varphi, \tilde{m})$, $\varepsilon = 0.1$

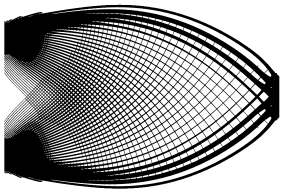

(m) $\tilde{\Omega}_\varepsilon(\varphi, \tilde{m})$, $\varepsilon = 0.05$

Figure 28: Complete process for a cantilever case

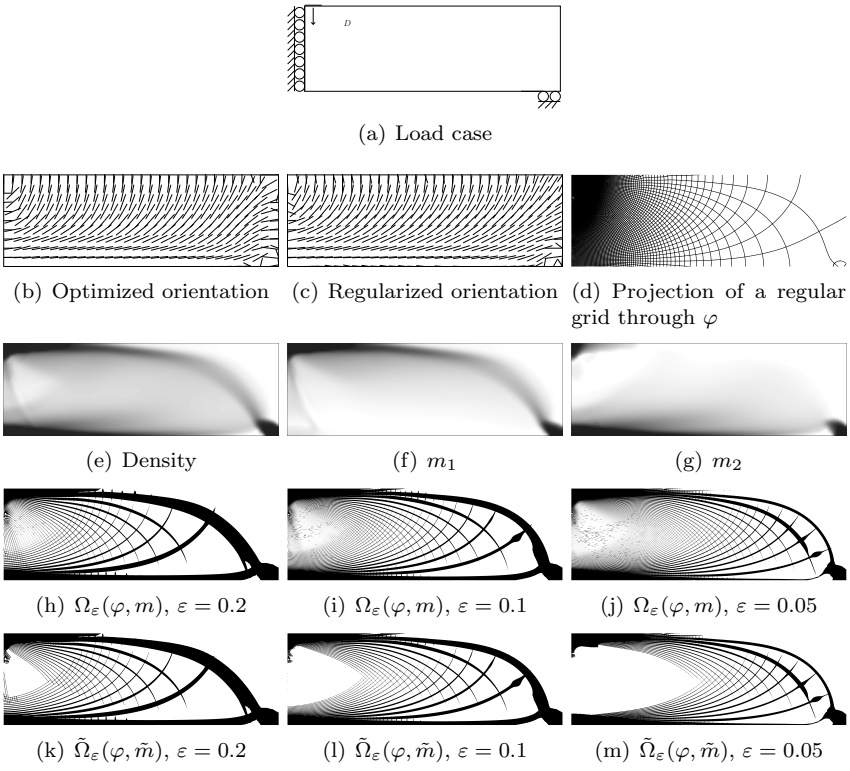

(a) Load case

(b) Optimized orientation (c) Regularized orientation (d) Projection of a regular grid through $\varphi$

(e) Density (f) $m_1$ (g) $m_2$

(h) $\Omega_\varepsilon(\varphi, m)$, $\varepsilon = 0.2$ (i) $\Omega_\varepsilon(\varphi, m)$, $\varepsilon = 0.1$ (j) $\Omega_\varepsilon(\varphi, m)$, $\varepsilon = 0.05$

(k) $\tilde{\Omega}_\varepsilon(\varphi, \tilde{m})$, $\varepsilon = 0.2$ (l) $\tilde{\Omega}_\varepsilon(\varphi, \tilde{m})$, $\varepsilon = 0.1$ (m) $\tilde{\Omega}_\varepsilon(\varphi, \tilde{m})$, $\varepsilon = 0.05$

Figure 29: Complete process for a MBB beam

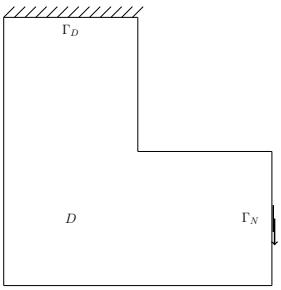


(a) Load case

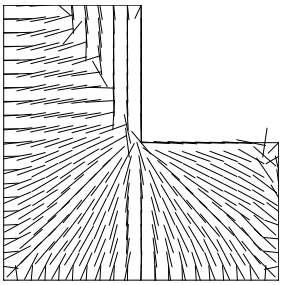

(b) Optimized orientation

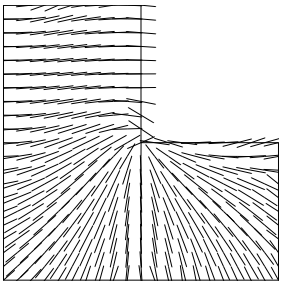

(c) Regularized orientation

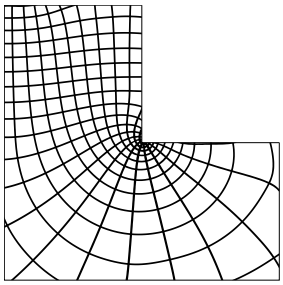

(d) Projection of a regular grid through $\varphi$

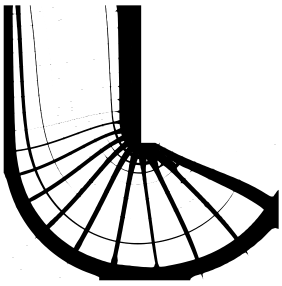

(e) $\Omega_\varepsilon(\varphi, m)$, $\varepsilon = 0.2$

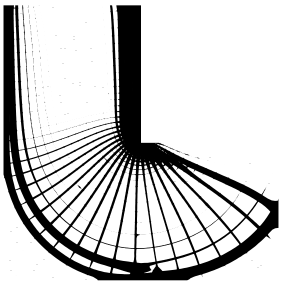

(f) $\Omega_\varepsilon(\varphi, m)$, $\varepsilon = 0.1$

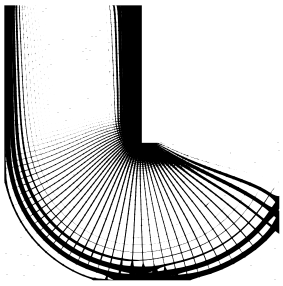

(g) $\Omega_\varepsilon(\varphi, m)$, $\varepsilon = 0.05$

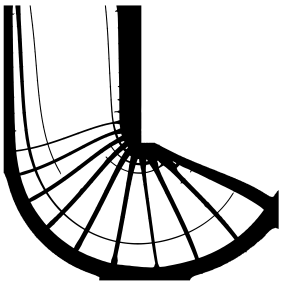

(h) $\tilde{\Omega}_\varepsilon(\varphi, \tilde{m})$, $\varepsilon = 0.2$

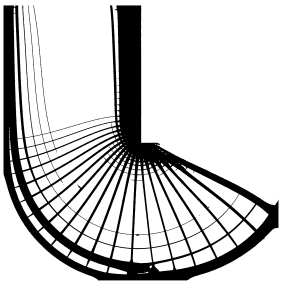

(i) $\tilde{\Omega}_\varepsilon(\varphi, \tilde{m})$, $\varepsilon = 0.1$

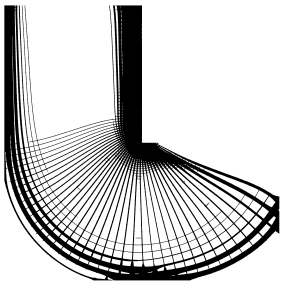

(j) $\tilde{\Omega}_\varepsilon(\varphi, \tilde{m})$, $\varepsilon = 0.05$

Figure 30: Complete process for a L-beam

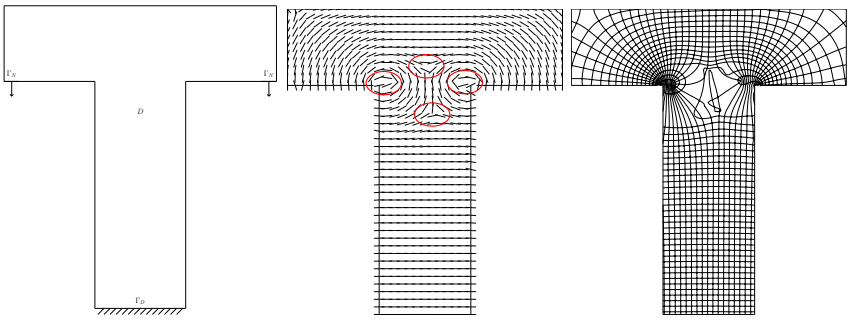

(a) Load case (b) Regularized orientation (c) Distorted grid

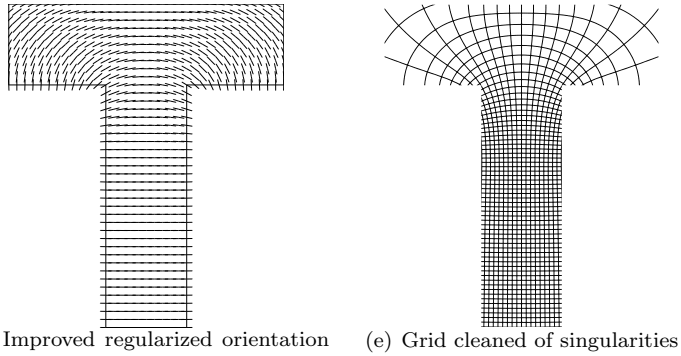

(d) Improved regularized orientation without anymore singularities (e) Grid cleaned of singularities

Figure 31: The electrical mast test case: singularities persist in the optimized orientation field, even after regularization

[9] J. Céa. Conception optimale ou identification de formes: calcul rapide de la dérivée directionnelle de la fonction coût. *RAIRO Modél. Math. Anal. Numér.*, 20(3):371–402, 1986.

[10] P. Geoffroy. *Homogenization method for topology optimization of structures built with lattice materials.* PhD thesis, École Polytechique, 91128 Palaiseau, France, to appear.

[11] J. Groen and O. Sigmund. Homogenization-based topology optimization for high-resolution manufacturable microstructures. *Internat. J. Numer. Methods Engrg.*, 113(8):1148–1163, 2018.

[12] J. Haslinger and J. Dvořák. Optimum composite material design. *ESAIM: M2AN*, 29(6):657–686, 1995.

[13] F. Hecht. New development in freefem++. *J. Numer. Math.*, 20(3-4):251–265, 2012.

[14] R. V. Kohn and G. Strang. Optimal design and relaxation of variational problems. I. *Comm. Pure Appl. Math.*, 39(1):113–137, 1986.

[15] K. A. Lurie, A. V. Cherkaev, and A. V. Fedorov. Regularization of optimal design problems for bars and plates. I, II. *J. Optim. Theory Appl.*, 37(4):499–522, 523–543, 1982.

[16] G. Michailidis. *Manufacturing Constraints and Multi-Phase Shape and Topology Optimization via a Level-Set Method.* PhD thesis, École Polytechique, 91128 Palaiseau, France, 2014.

[17] F. Murat and L. Tartar. Calcul des variations et homogénéisation. In *Homogenization methods: theory and applications in physics (Bréau-sans-Nappe, 1983)*, volume 57 of *Collect. Dir. Études Rech. Élec. France*, pages 319–369. Eyrolles, Paris, 1985.

[18] O. Pantz and K. Trabelsi. A post-treatment of the homogenization method for shape optimization. *SIAM J. Control Optim.*, 47(3):1380–1398, 2008.

[19] O. Pantz and K. Trabelsi. Construction of minimization sequences for shape optimization. In *Methods and Models in Automation and Robotics (MMAR), 2010 15th International Conference on*, pages 278 –283, 8 2010.

[20] P. Pedersen. On optimal orientation of orthotropic materials. *Structural optimization*, 1(2):101–106, 1989.

[21] O. Sigmund and J. Petersson. Numerical instabilities in topology optimization: A survey on procedures dealing with checkerboards, mesh-dependencies and local minima. *Structural optimization*, 16(1):68–75, 1998.

[22] P. Zhang, J. Toman, Y. Yu, E. Biyikli, M. Kirca, M. Chmielus, and A. C. To. Efficient design-optimization of variable-density hexagonal cellular structure by additive manufacturing: theory and validation. *Journal of Manufacturing Science and Engineering*, 137(2):021004, 2015.

[23] M. Zhou and G. Rozvany. The coc algorithm, part ii: Topological, geometrical and generalized shape optimization. *Computer Methods in Applied Mechanics and Engineering*, 89(1–3):309 – 336, 1991. Second World Congress on Computational Mechanics.